

Biomedical Image Processing and Classification

Original

Biomedical Image Processing and Classification / Mesin, Luca. - STAMPA. - (2021). [10.3390/books978-3-0365-0347-9]

Availability:

This version is available at: 11583/2916357 since: 2021-08-03T10:18:44Z

Publisher:

MDPI

Published

DOI:10.3390/books978-3-0365-0347-9

Terms of use:

This article is made available under terms and conditions as specified in the corresponding bibliographic description in the repository

Publisher copyright

(Article begins on next page)

2. Materials and Methods

Two different brain slice datasets were used in this work. Firstly, the real-world clinical dataset, which comprises 22 brain slices (axial T2 MR DICOM slices), obtained from the Proscans Diagnostics Centre (Chennai, India). Secondly, the benchmark BRATS dataset was used for evaluating the performance of the proposed model. Further, in this work, the BRATS dataset comprised of ten patients and around 200 brain slices were acquired from each patient. This section specifies that the proposed approach was deployed to segment and analyze the axial MR DICOM slices. Initially, the DICOM slices are subjected to pre-processing. The segmentation of preprocessed DICOM slices is subjected to fuzzy clustering for image enhancement. In order to select the best clusters, the silhouette metric is employed. The enhancement of extracted structures is carried out using morphological operations. Finally the ROI is extracted using image post-processing procedures such as MCW, RG, and DRLS, and the extracted tumor is validated using similarity measures. The complete architecture is shown in Figure 1. Also volumetric quantification of tumor and 3D visualization is generated from the slices involved in the real-time clinical study. The decision making capability of the proposed approach is tested and validated using 2D slices of the considered image dataset.

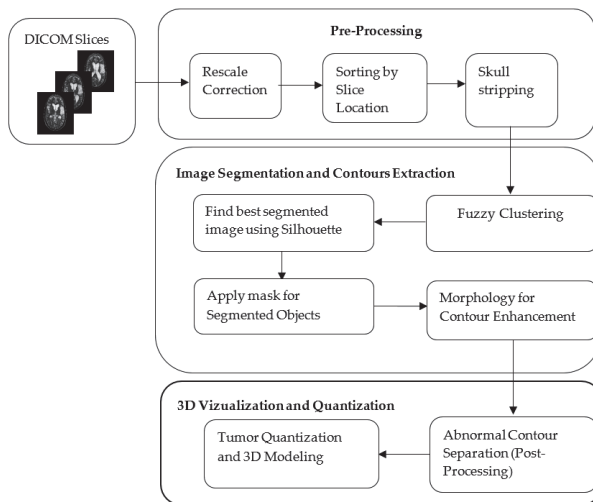


Figure 1. The Architecture of the Proposed Hybrid Model.

2.1. Pre-Processing

The considered slices are presented to the system as (.dcm) files. Rescale correction is performed on all the slices which provide a 512*512 pixel array for each image. The DICOM tags Rescale Intercept (RI) and Rescale Slope (RS) postulates the linear transformation of pixels to their memory representation. The Rescale Correction [36] of the slices is given by:

$$RC = I * RS + RI \quad (1)$$

where RC is the rescaled units, I is the intensity value. In MR DICOM metadata, the attributes rescale slope and rescale intercept are not available as tags. For the computational purpose, the tag values are engaged as one and 1024, respectively. The available slice location header attribute in MR allows brain slices to be added for processing sequentially.

Abnormality identification in the brain requires removal of the skull or non-brain tissues such as dura, arachnoid, pia mater for effective extraction of ROI. The skull portions possess a low solidity area. Solidity is the proportion of the contour area to its convex hull area. Regions having the least solidity

are removed, leaving only the region occupied by the actual brain tissue. The slices which have high solidity objects were retained after rescaling correction, thereby eliminating the non-brain matter.

2.2. Fuzzy Clustering Based Object Extraction from DICOM Slices

The fuzzy clustering (FC) technique is performed to extract the best segmentation in a feature space containing varying cluster intensities and shapes. Fuzzy clustering classifies a set of data points $p_1, p_2, p_3, \dots, p_m$ of a DICOM slice into k ($\leq m$) clusters, which minimizes the total distortion. Each data point in the feature space has a degree of membership (a_{ij}) to its own cluster. The points closest to cluster centroids has a higher degree compared to the points in the cluster edge. For a data point i assigned to cluster j , gives a_{ij} coefficient value for being in the j th cluster. The sum of a_{ij} coefficient is always 1. The fuzzy assisted clustering algorithm based on minimization of the following objective function (F_w) concerning A (fuzzy k partition) and B (k set of clusters) and it is given by:

$$F_w(A, B) = \sum_{j=1}^m \sum_{i=1}^k (a_{ij})^w d^2(P_j, B_i); k \leq m \quad (2)$$

where, $w(>1)$, is the weighting exponent acts as a control parameter for the fuzziness in a_{ij} , P_j is the j^{th} point in the feature vector of N -dimensional space, B_i being the centroid for cluster i , a_{ij} is the degree of membership of the pixel P_j in cluster i , $d^2(P_j, B_i)$ is the distance measure between P_j and B_i , m and k represent the number of data points and the number of clusters, respectively.

The degree of membership of all feature vectors is associated with the inverse of the distance to the cluster center:

$$a_{ij} = \frac{\left[\frac{1}{d^2(P_j, B_i)} \right]^{1/w-1}}{\sum_{i=1}^k \left[\frac{1}{d^2(P_j, B_i)} \right]^{1/w-1}} \quad (3)$$

The Euclidean distance measure is used to compute the degree of membership (a_{ij}) is given as:

$$d^2(P_j, B_i) = (P_j - B_i)^T I (P_j - B_i) \quad (4)$$

where I denotes the identity matrix. The new centroid positions are computed based on the mean of all the points, weighted by its corresponding degree of membership (a_{ij}) to the cluster:

$$\widehat{B}_i = \frac{\sum_{j=1}^n (a_{ij})^w P_j}{\sum_{j=1}^n (a_{ij})^w} \quad (5)$$

Based on new centroid positions the updated degree of membership (\widehat{a}_{ij}), is computed according to a_{ij} shown in Equation (3). This process is repeated until the sum of distances of each point in the slice to the centroid of the cluster is minimum, i.e., a termination criterion ' ϵ ' is reached, which ensures maximum accuracy. Other stopping criteria include no further improvement in the variance over some iterations. The structures of the brain are segmented from the set of DICOM slices for a set of ' k ' values ranging from 2 to 9.

2.3. Selection of the Best (k) Using Silhouette Index

Fuzzy clustering renders the clustered image for the preferred number of clusters (k). However, optimal ' k ' should be chosen in order to place cluster labels within the centroid. In literature, a well-balanced coefficient named silhouette score, presented by Rousseeuw [37], has shown higher performance in finding optimal clusters. The silhouette score pertains to the deviation between the within-class tightness and separation. Specifically, the silhouette value for a pixel in the slice pixel array is given by,

$$sil(j) = \frac{b(j) - a(j)}{\max(a(j), b(j))} \quad (6)$$

where, $a(j) = 1/|V_i| - 1 \sum_{y \in V_i} d(x, y)$, be the mean distance of pixel point 'x' with other pixels (y) within the cluster V_i and $b(j) = \min \{1/V_i \sum_{y \in V_i} d(x, y)\}$, be the average dissimilarity of a point 'x' to about any cluster V_i of which chosen point 'y' is not associated with it.

The maximum value of $s(j)$ reflects the optimal number of clusters. Correspondingly, the minimum of $b(j)$ is taken for computing $s(j)$. If $b(j)$ is larger, then the point is very far from its next neighboring cluster. The squared Euclidean distance provides the distance metric $d(x, y)$ between clusters for computing the silhouettes.

K-means clustering with silhouette analysis is executed to find out the optimal 'k' ranging from 2 to 9.

Silhouette always lies between -1 to 1 , and it is defined as:

$$sil(j) = \begin{cases} 1 - a(j)/b(j), & \text{if } a(j) < b(j) \\ 0, & \text{if } a(j) = b(j) \\ b(j)/a(j) - 1, & \text{if } a(j) > b(j) \end{cases} \quad (7)$$

If the silhouette values are approaching either $+1$ or -1 , the pixel points are well clustered or misclassified, respectively. If zero, the points could be assigned to another cluster also.

Further, to validate the segmented slices, the entire pixel array of each slice is considered, and the average silhouette width is computed. The average silhouette width for every slice is calculated from mean of all the distinct cluster silhouettes is given by:

$$S_{avg}(s_i) = \frac{\sum_i^n sil(j)}{k} \quad (8)$$

where, n denotes the number of clusters segmented. The S_{avg} is used to find the best k for a slice s_i . The silhouette coefficient ($k_{best,i}$) is defined as the maximum average silhouette width which is given by,

$$k_{best,i} = \max\{S_{avg}(s_i)\} \quad (9)$$

The algorithmic steps of incorporating fuzzy clustering and silhouette metric to the set of DICOM slices are illustrated in Algorithm 1.

Algorithm 1 Silhouette-enabled Fuzzy Clustering

- 1: Let $S = \{s_1, s_2, s_3, \dots, s_m\}$ (Set of Dicom Slices)
 - 2: $P = \{p_1, p_2, p_3, \dots, p_m\}$ (Set of data points to be clustered)
 - 3: $K_r, r \in \text{cluster_range } [2:10]$
 - 4: $k_{best} = \text{Best K value of the clustered image}$
 - 5: $B = \{b_1, b_2, b_3, \dots, b_k\}$ (Set of cluster Centroids)
 - 6: for each $s_i \in S$
 - for each k in K_r
 - for each $p_i \in P$
 - Compute fuzzy Clustering by iteratively updating the degree of membership (a_{ij}) and cluster centroids \hat{B}_i
 - end
 - 7: for every k in S_i
 - 8: Compute averagesilhouettewidth from individual cluster silhouettes (finding best k from r)
 - 9: end
 - 10: Compute $k_{best,i} = \max(\text{averagesilhouettewidth})$ (Calculate k_{best} for Slice i)
 - 11: End
-

2.4. Morphological Operations for Objects Enhancement

Image masking is used to specify the foreground, background, or probable background/foreground. Contour masking separates the objects from the original images, and it is essential for further analysis. It is eliminating the outliers such as air, from the actual brain slices. The fuzzy clustering process discovers the best-segmented clusters. These clusters form a binary mask that overlaid on the actual slices to acquire the respective contour intensities. Mutual information (I) is computed between the contour mask with the corresponding slice for ensuring similarity [38,39]. The weighted contribution (W_i) of the contour mask (CM_i) to the original slice (S_i) is calculated as:

$$W_i = \frac{1}{CM_i} e^{-\frac{I_i - I_{min}}{I_{max} - I_{min}}} \quad (10)$$

where I_i represents the mutual information between CM_i and S_i . I_{max} , I_{min} are the maximum and minimum mutual information for the overall CM_i . After the extraction of structures from the fuzzy clustering process, the obtained binary mask of the chosen slices may be distorted due to noise and texture. Mathematical morphology, a kind of contrast enhancement technique, assists selective enhancement of the small diagnostic contour features that are overlaid on a composite background. Hence, the binary mask representing the extracted structures is further practiced with non-linear operations such as morphological erode and morphological dilate for removing the inadequacies in order to retain the form and structure of the extracted objects. Erosion is a reverse process to dilation-erosion strips pixel layer over the edges, contradictorily dilation augments pixel layer over the edges.

Dilation adds pixels to the contour boundaries in the slices. The number of supplementary pixels integrated into the mask image is subject to the shape and size of the structuring element. Dilation process is done by:

$$CM \oplus SE = \{z | (\widehat{SE})_z \cap CM \neq \varphi\} \quad (11)$$

where CM is the set of pixels representing the binary mask, SE be the structuring element initially reflected as \widehat{SE} then the reflected element is translated by z . This process enlarges the binary mask in all directions not to miss any pixels, particularly at contour edges. Similarly, erosion is performed by:

$$CM \ominus SE = \{z | (SE)_z \subseteq CM\} \quad (12)$$

Stating that z confined in CM shifts the SE . Erosion removes pixels, thus sharpening the object boundary. The number of pixels stripped is subject to the size of the SE . Erosion strips the connected normal and abnormal contours, which aid in the effective extraction of ROI in the post-processing stages.

2.5. Tumor Quantization and Validation

The extracted objects possess high solidity ventricles and the tumor region. In order to extract the ROI from the brain structures, image post-processing approaches are utilized to mine the ROI from the extracted objects. After determining the abnormal regions, the size of the tumor is quantified based on its area and perimeter.

The validation metrics are used to evaluate the spatial intersection of ground truth (GT) of the clinical slices with the extracted ROI [40]. The performance of the segmentation procedure is validated using similarity measures such as Dice, Jaccard, false positive (FPR), and false negative (FNR) rates.

These measures are mathematically conveyed as:

$$Jaccard(I_{gt}, I_{ROI}) = (I_{gt} \cap I_{ROI}) / (I_{gt} \cup I_{ROI}) \quad (13)$$

$$Dice(I_{gt}, I_{ROI}) = 2(I_{gt} \cap I_{ROI}) / (I_{gt} \cup I_{ROI}) \quad (14)$$

$$FPR(I_{gt}, I_{ROI}) = (I_{gt} / I_{ROI}) / (I_{gt} \cup I_{ROI}) \quad (15)$$

$$FNR(I_{gt}, I_{ROI}) = (I_{ROI}/I_{gt}) / (I_{gt} \cup I_{ROI}) \quad (16)$$

where, I_{gt} expresses to the ground truth (GT) and I_{ROI} points for the segmented image with the proposed strategy. Other related works implemented on brain MRI can be found in [41–49].

2.6. Volume Assessment and 3D Modeling

The clinical slices considered in this work have the cubical stack format $[SC \times W \times H]$, SC signifies the number of slices (22), W, and H indicates the width and height of a slice $[512 \times 512]$ in pixels, respectively. The slices are processed in DICOM format, which holds adequate slice information. In DICOM metadata, it is identified that ‘slice thickness (ST)’ is 5 mm, ‘pixel spacing (PS_x/PS_y)’ is (0.4492 mm/0.4492 mm) and ‘spacing between slices (SS)’ is 6.5 mm. The original stack $[22 \times 512 \times 512]$ migrated to a resampled stack $[110 \times 230 \times 230]$ based on the spacing information presented in the DICOM header. Resampling is achieved by cubic spline interpolation function. The tumor volume is estimated as:

$$Volume = Tumor\ Voxels * Voxel\ size \quad (17)$$

where tumor voxels are the number of voxels that contributes to tumor and voxel size is measured based on pixel spacing and slice thickness.

Visualization of tumor voxels in the complete study is achieved by merging the tumor containing slices to form a voxel mesh in all three anatomical planes. Further, this exemplifies an interconnected set of triangular faces of tumor voxels [50].

3. Results and Discussions

This section illustrates the results achieved with the proposed procedure. Figure 2 demonstrates a brief overview of the proposed procedure for brain MR examination. Initially, the DICOM slices of the patient study are pre-processed with rescaling correction. Moreover, this creates the intensity of the similar tissues in the study to confirm across the image slices. Then the non-brain tissues are stripped from the brain matter, leaving the brain pixels, which contain the brain tissues. Figure 3 shows the representative image of slice 12 before extraction (a) of brain tissue after removing (b) the non-brain portions. This procedure avoids non-brain tissues to add unnecessary information, thereby enhancing the efficacy of extracting the ROI. The combination of Fuzzy clustering with validated silhouette index (as the criterion for choosing best k) discovers the precise number of clusters from the slices. Figure 4 shows the extracted objects of Slice-14 and its corresponding mask image for ‘k’ clusters (k ranges from 2 to 9).

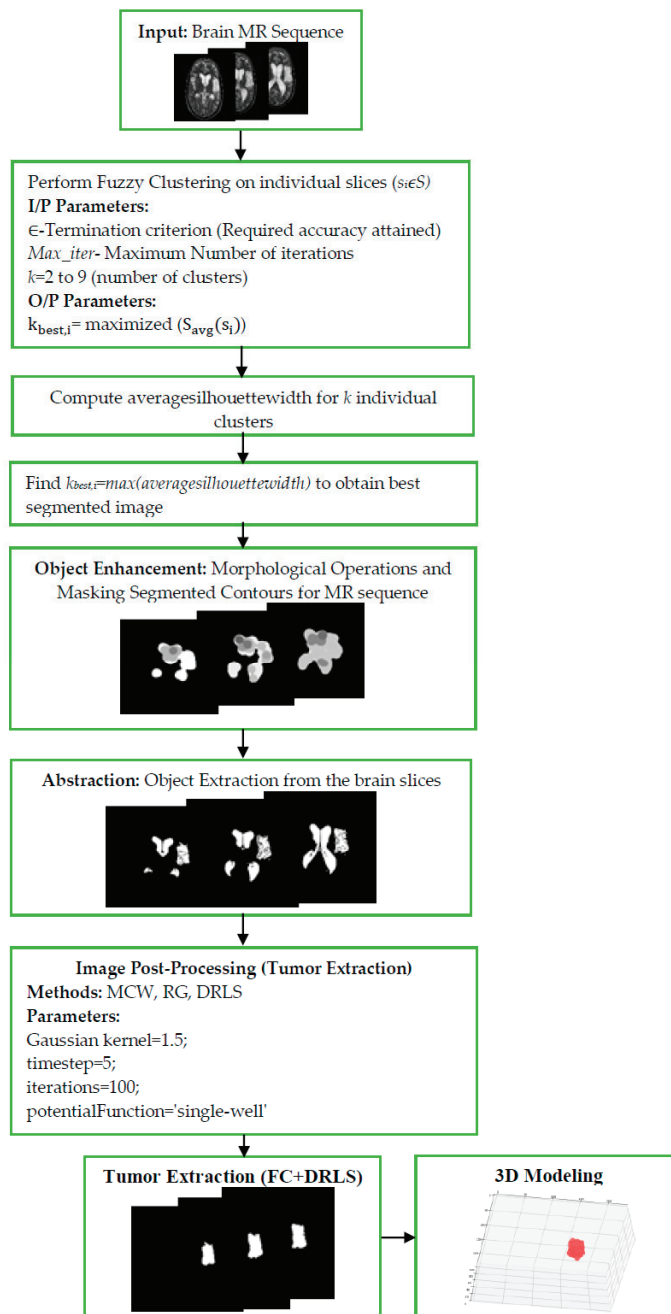
Table 1 shows the silhouette scores S_{avg} for the considered slices for the chosen k values. A more substantial silhouette value gives a high split over the data points. For slice10 in Table 1, the optimal k is elected as two, since $S_{avg}(s_i)$ holds the maximum value 0.45571. Similarly, the optimal $k_{best,i}$ is selected from the range of slices (Slice11–Slice14) based on the average silhouette width.

Table 1. Silhouette scores for Slices (10–14).

Slices	k = 2	k = 3	k = 4	k = 5	k = 6	k = 7	k = 8	k = 9
Slice 10	0.45571	0.37847	0.3974	0.40063	0.40432	0.40568	0.411	0.35408
Slice 11	0.42842	0.41451	0.44141	0.43435	0.43878	0.4262	0.43644	0.43349
Slice 12	0.44109	0.45273	0.4498	0.46001	0.47158	0.4616	0.46032	0.46397
Slice 13	0.47107	0.50479	0.51933	0.50445	0.51069	0.50843	0.50041	0.43237
Slice 14	0.48988	0.53767	0.54796	0.55355	0.58523	0.53146	0.52066	0.52847

The maximum silhouette score ($k_{best,i}$) obtained for the cluster range are highlighted in **bold**.

In slice14 the maximum $S_{avg}(s_{14}) = 0.58523$ when k is six, but a minimum value resulted when k is two, ($S_{avg}(s_{14}) = 0.48988$). Further, this shows the loss of tumor information in Figure 4 when k is two, and an optimal segmentation is obtained when k is six.



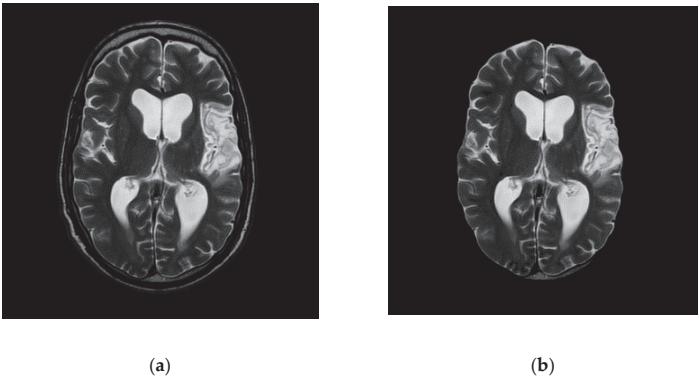


Figure 3. Slice (12) Before (a) and after (b) skull stripping.

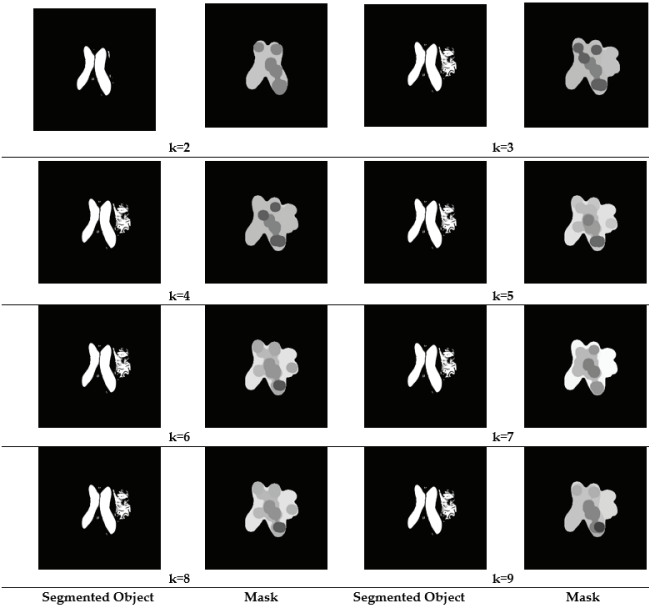


Figure 4. Segmented results and Masked Objects for Slice 14.

Figure 5a shows the graph with silhouette scores versus the number of clusters ‘ k ’ for a representative sample image ‘slice14.dcm’. The average silhouette width for the slices, which are more than 0.48, confirms a good split for all k clusters. As shown in the graph, a reasonable peak is obtained when $k = 6$ and also possess a maximum value ($S_{avg}(s_{12}) = 0.58523$).

Figure 5b depicts the silhouette plot for slice14. The selection of an optimal k provides better separation in feature space with more similar thickness and sizes. This increase in $S_{avg}(s_{14})$ is due to the distinct separation from their neighboring clusters except for the background. The well-diversified information is obtained from the slices since the proper selection silhouette index was made. From the achieved outcomes, it is clear that silhouette analysis plays a significant role in the identification of best-clustered objects. After FC, the pixels representing abnormalities are spatially identified and segmented. The mask image is produced from the objects extracted from each slice, in order to distinguish from outliers/background. The mask image holds the pixel intensity values of abnormal

and normal pixel intensities. The mask is applied to the corresponding slice for the extraction of clustered intensities from the actual slices. The objects are further enhanced by morphological processes by performing morphological open, dilate, erode and close operations in a sequential order to obtain a smoother object boundary without speckles. The experimental results of Figure 3 confirms a superior image enhancement step; as a result, it shows the best separation of objects obtained from composite backgrounds.

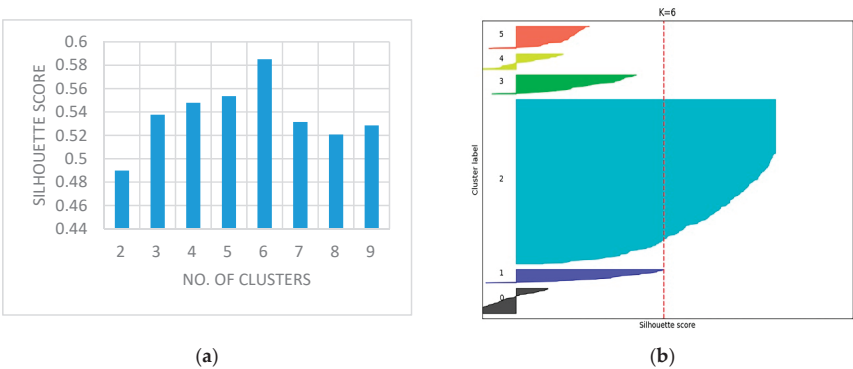



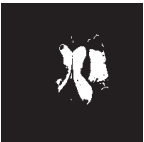













Figure 5. (a) No. of Clusters vs. Silhouette Scores; (b) Silhouette plot for Slice-14.

Each slice in the MR sequence is distinctly examined using the eminent state-of-art segmentation methods such as watershed [51], Chan-Vese [52], and fuzzy clustering (FC). The image quality measures obtained from these methods are portrayed in Table 2. From the segmented results of FC, it is perceived that FC based segmentation offers distinct separation of objects and aids a better confidant for the image post-processing stages.

Table 2. Segmented results for state-of-art segmentation methods.

	Slice 10	Slice 11	Slice 12	Slice 13	Slice 14
Watershed					
Chan-Vese					
Fuzzy Clustering					

Further, for measuring the supremacy of the segmentation approaches, the well-known image quality measures [53] such as peak signal to noise ratio (PSNR), normalized cross-correlation (NCC),

normalized absolute error (NAE) and structural similarity index (SSIM) are calculated and are presented in Table 3. From the table values, it is perceived that the FC method discovers the vital prominent structures and thus preserves the segmentation quality. Also, the average image quality measures attained through FC is superior compared to the other state-of-art approaches reflected in this work.

Table 3. Image quality measures for segmentation methods.

Segmentation	Slice	PSNR	NCC	NAE	SSIM
Watershed	Slice 10	21.3173	0.4923	0.6852	0.7955
	Slice 11	19.8605	0.3846	0.7571	0.7095
	Slice 12	22.6953	0.4742	0.7021	0.6992
	Slice 13	20.8065	0.4192	0.7121	0.7148
	Slice 14	21.7631	0.4031	0.7231	0.7219
	Average	21.28854	0.43468	0.71592	0.72818
Chan-vese	Slice 10	24.0187	0.5102	0.6712	0.7083
	Slice 11	23.0823	0.5802	0.6328	0.7153
	Slice 12	22.0176	0.4979	0.6693	0.6983
	Slice 13	25.2131	0.5374	0.6501	0.7213
	Slice 14	23.0129	0.5278	0.6712	0.6859
	Average	23.46892	0.5307	0.65892	0.70582
Fuzzy Clustering	Slice 10	20.9234	0.4865	0.7091	0.6995
	Slice 11	28.6764	0.7681	0.4065	0.8204
	Slice 12	30.5289	0.7548	0.3773	0.8143
	Slice 13	32.3411	0.7917	0.3961	0.8968
	Slice 14	31.5401	0.7842	0.3843	0.8412
	Average	28.80198	0.71706	0.45466	0.81444

The proposed approach had been tested for its performance by validating it against the grand challenge benchmark image dataset called the BRATS (size: 236×216 pixels). In this dataset, ten patient studies of T2 and T1C modalities had been taken up for analysis, which contains axial brain MR image series. The sample image series of patient studies and their corresponding GT that are obtained are shown in Figure 6. The BRATS dataset that had been considered in the proposed research has a number of advantages, few of those are—The desirable amount of 2D slices of a patient study can be easily extracted from its skull stripped 3D brain MRI, modalities like Flair, T1, T1C, and T2 are easily supported, contains ground truth images for all modalities offered by an expert member. Due to these reasons that most researchers had adopted the BRATS images for testing their disease examination tool.

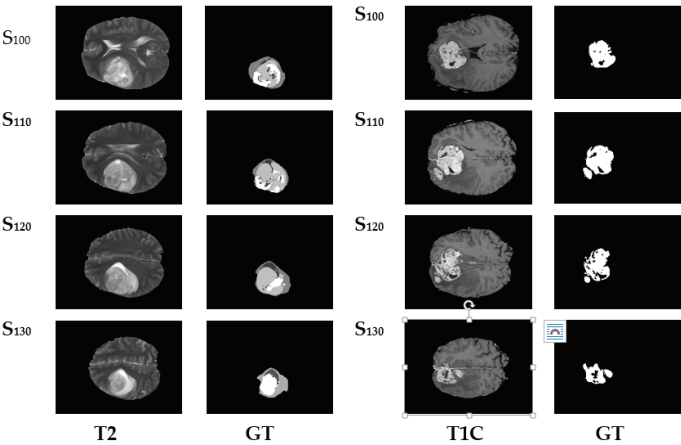


Figure 6. BRATS Dataset image series with Expert’s Ground Truth.

For a comparative analysis in the post-processing stage, the ROI mining technique, marker controlled watershed segmentation (MCW), Seed region growing (RG) and distance regularized level sets (DRLS) are adopted and implemented to extract the anomalous section from the segmented objects (shown in Figure 4). MCW is a well-known segmentation technique associated with marker controlled morphological function and Sobel's edge detection. This procedure detects ROI with the assistance of priori provided whole alike image intensities [54].

In contrast to MCW, the level sets the implicit active contour models, uses gradient information of the image, and thus naturally handles topological deviations by merging or splitting the contours [55]. The parameters for DRLS is assigned as follows; number of iterations = 100, scale parameter = 1.5, potential function = single-well and timestamp = 5.

RG is an operator instigated semi-automated method, extensively used to extract the desired (abnormal) structures from medical images [56]. RG requires a seed point (pixel position) to be initialized somewhere within a contour or ROI. From the seed point, the RG procedure will start mining the similar intensities of possible connected neighboring pixels accessible in the ROI.

The images chosen are initially subjected to FC for objects enhancement before applying the post-processing. The image quality gets enhanced through the validated FC technique and provides an ideal platform for the post-processing that is performed using MCW, RG, and DRLS. Figure 7 depicts the brain abnormality segmentation results extracted from the 2D slices of T2 modality images through FC assisted MCW, RG, and DRLS techniques. Correspondingly, results of segmented ROI from 2D slices of T1C modality are shown in Figure 8.

The segmentation methods (MCW, RG, and DRLS) that had been implemented were assessed for their performance by carrying out a comparative analysis that was executed between the ROI and GT. The extracted ROI and GT were initially compared on T2 modality images, followed by T1C modality images. The results obtained from these comparisons were recorded in Tables 4 and 5. The recordings were made based on image similarity measures like Jaccard, Dice, FPR, and FNR. Figure 9 shows the comparative analysis of assessed similarity measures of T2 and T1C weighted images. The corresponding average scores of Tables 4 and 5 are depicted in the graph.

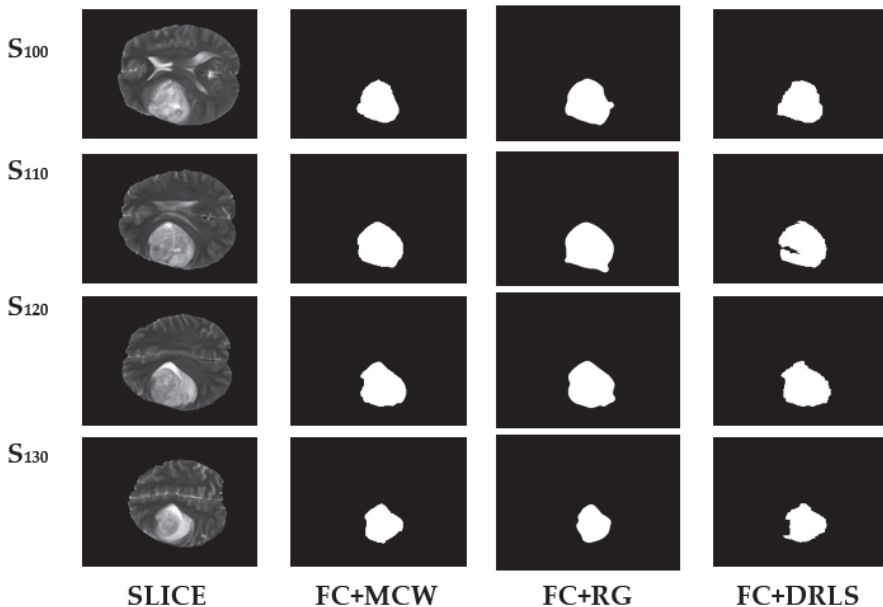


Figure 7. Segmentation results of BRATS T2 series.

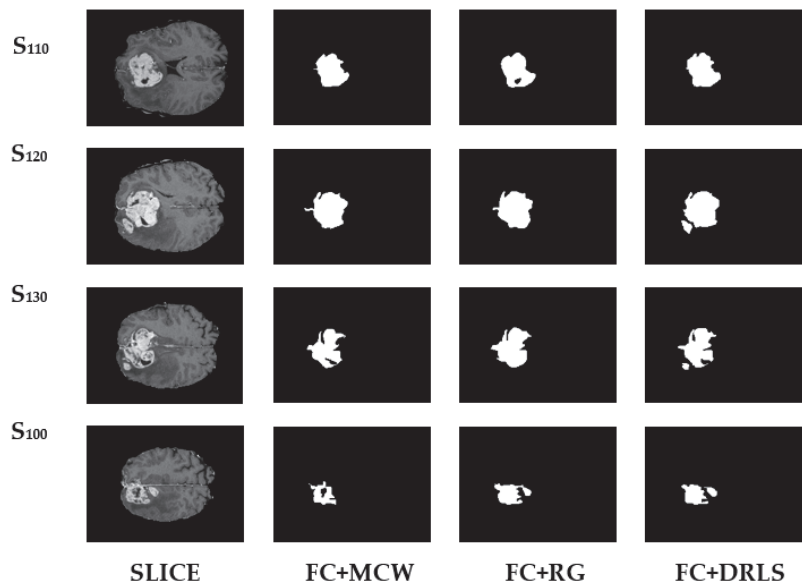


Figure 8. Segmentation results of BRATS T1C series.

Table 4. Image similarity measures for BRATS T2 MRI series.

	Slice	Jaccard	Dice	FPR	FNR
FC+MCW	S ₁₀₀	0.8625	0.9201	0.00617	0.0487
	S ₁₁₀	0.7623	0.8587	0.00126	0.1327
	S ₁₂₀	0.7162	0.828	0.00427	0.1117
	S ₁₃₀	0.7428	0.7048	0.002044	0.2123
FC+RG	S ₁₀₀	0.8914	0.9421	0.00796	0.0742
	S ₁₁₀	0.7785	0.8691	0.00127	0.1566
	S ₁₂₀	0.7189	0.8299	0.00144	0.1951
	S ₁₃₀	0.7478	0.7868	0.00923	0.3995
FC+DRLS	S ₁₀₀	0.8958	0.9334	0.00288	0.083
	S ₁₁₀	0.7939	0.9091	0.00119	0.179
	S ₁₂₀	0.7427	0.8525	0.00176	0.1925
	S ₁₃₀	0.7592	0.7951	0.00159	0.2636

Table 5. Image similarity measures for BRATS T1C MRI series.

	Slice	Jaccard	Dice	FPR	FNR
FC+MCW	S ₁₀₀	0.6645	0.8284	0.0047	0.1904
	S ₁₁₀	0.5154	0.9067	0.0064	0.1868
	S ₁₂₀	0.6923	0.8643	0.0069	0.1628
	S ₁₃₀	0.7187	0.8322	0.0061	0.1954
FC+RG	S ₁₀₀	0.7071	0.9123	0.0051	0.1962
	S ₁₁₀	0.8293	0.8045	0.0058	0.1895
	S ₁₂₀	0.761	0.8999	0.0052	0.1552
	S ₁₃₀	0.7127	0.9034	0.0043	0.2001
FC+DRLS	S ₁₀₀	0.7628	0.8655	0.0054	0.2467
	S ₁₁₀	0.8376	0.9116	0.0057	0.0994
	S ₁₂₀	0.8187	0.9003	0.0059	0.1567
	S ₁₃₀	0.7357	0.8477	0.0054	0.1886

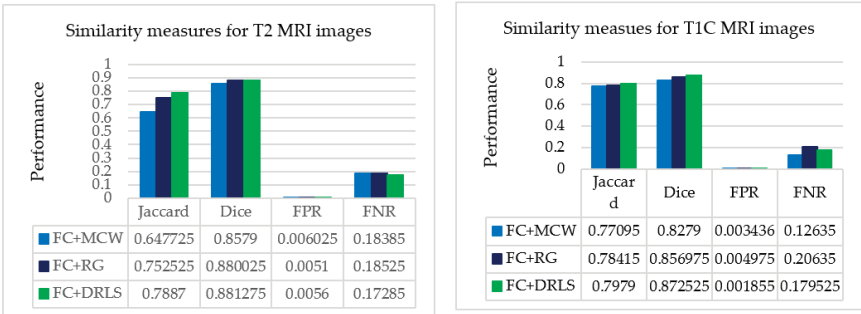


Figure 9. Average picture similarity measures of a patient study against expert’s ground truth.

From the recorded values for the considered slices presented in Tables 4 and 5, it could be inferred that the outcome produced through FC based DRLS technique is far more superior to FC+MCW and FC+RG techniques. Also, the metrics Jaccard and Dice are computed for ten patient studies of BRATS individually. Figures 10 and 11 depicts the average scores for ten patient studies of the BRATS dataset, and ‘Av.’ represents the overall average score of all the patient studies from T2 and T1C weighted images, respectively.

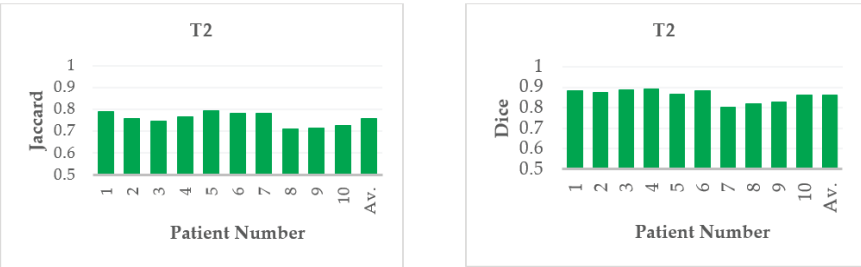


Figure 10. Average Jaccard and Dice score of individual patient studies for T2 modality. ‘Av.’ specifies the average score of all the patient studies.



Figure 11. Average Jaccard and Dice score of individual patient studies for T1C modality. ‘Av.’ Specifies the average score of all the patient studies.

Furthermore, the suggested procedure is attempted on clinical MRI brain study of a patient [57]. The patient study considered contains axial T2 MR DICOM slices. The DICOM slices between the ranges Slice-10 to Slice-14 are considered in this approach for tumor analysis, as they hold enough tumor information. Slice15 and above are excluded from the examination as it does not contain any tumor region. Initially, the considered series are enhanced using FC, then at the post-processing stage,

the mining techniques MCW, RG, and DRLS are adopted. Figure 12a,b embody the slice number with an optimal k and the original (actual) middle slices. Figure 12c represents the ground truth provided by an expert member. Figure 12d–f signify the ROI extracted from the validated fuzzy clustering-assisted MCW, RG, and DRLS procedures.

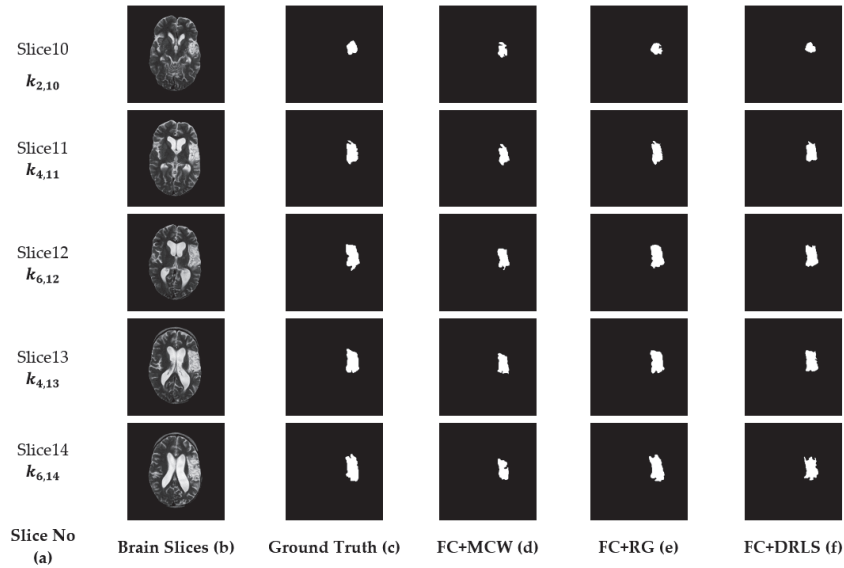


Figure 12. Segmented results of the clinical dataset (middle slices only).

The validation of the FC-aided mining procedures against GT images is performed using well-known image similarity measures such as Dice, Jaccard, false-negative, and false-positive rates. These parameters stay as an aid to assess the efficacy of the segmentation procedure.

From Table 6, it is observed that maximum similarity is attained between ROI and GT by the suggested FC+DRLS procedure shown on the Jaccard and Dice metric scores. FPR values indicate that typical pixels of the brain are misclassified as tumor pixels. Similarly FNR values depict pixels which contribute as tumor are misclassified as normal pixels of the brain.

Table 6. Image similarity measures for clinical T2 MRI series.

	Slice	Jaccard	Dice	FPR	FNR
FC+MCW	S ₁₀	0.6932	0.7832	0.1027	0.0612
	S ₁₁	0.8223	0.8828	0.1075	0.0311
	S ₁₂	0.8185	0.8569	0.1579	0.0424
	S ₁₃	0.8137	0.8761	0.1683	0.0422
	S ₁₄	0.7314	0.8168	0.1544	0.1201
FC+RG	S ₁₀	0.7209	0.7767	0.1123	0.0723
	S ₁₁	0.8149	0.8934	0.1099	0.0793
	S ₁₂	0.7953	0.8491	0.1184	0.0683
	S ₁₃	0.8054	0.7962	0.1163	0.0923
	S ₁₄	0.7821	0.8021	0.1201	0.0876
FC+DRLS	S ₁₀	0.6874	0.7949	0.1336	0.0642
	S ₁₁	0.8104	0.8972	0.1253	0.032
	S ₁₂	0.8256	0.8625	0.1368	0.0296
	S ₁₃	0.8179	0.8879	0.1374	0.038
	S ₁₄	0.7555	0.8596	0.1164	0.0958

The minimum values of FPR and FNR guarantee the efficiency of the FC+DRLS segmentation method against MCW and RG in the set of DICOM slices. Figure 13 shows the comparative analysis of assessed similarity measures using the average scores of the slices depicted in Table 6. Therefore it is evident that in the proposed approach, the FC+DRLS based segmentation technique produces superior results for the clinical study as well.

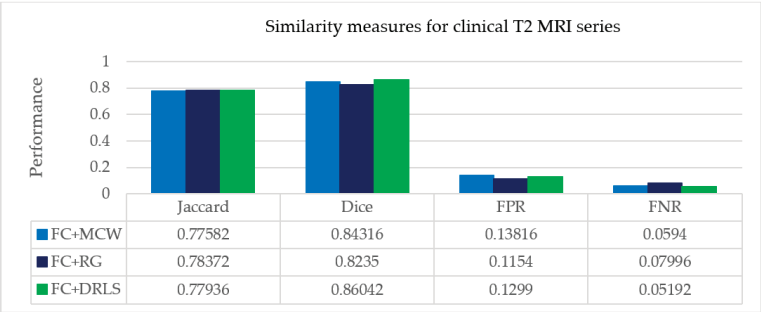












Figure 13. Average picture similarity measures of clinical study with expert’s ground Truth.

Further, the ROI (tumor) is extracted to acquire the geometrical properties such as area and perimeter. The captured tumor information is clearly visible from slice10 to slice14. In Table 7, the parameters, area, and perimeter are calculated based on the tumor information extracted from the ROI. The parameters gradually increase up to slice13, which holds the maximum tumor part and then decreases. The overall study of a patient is determined from the entire DICOM slices.

Table 7. Quantization features Area and Perimeter for best ‘K’.

Slices	FC Enhancement	ROI by DRLS	Area	Perimeter
Slice 10 (k = 2)			2268	192.5097
Slice 11 (k = 4)			4842	324.60
Slice 12 (k = 6)			6090	366.74
Slice 13 (k = 4)			6091	375.90
Slice 14 (k = 6)			6008	320.1680
(a)	(b)	(c)	(d)	(e)

The slices are reconstructed to a cubical stack based on in-stack position attribute of DICOM. The extracted objects of the clinical study undergo volumetric estimates and 3D reconstruction. Table 8 shows the volume of tumor calculated for DICOM and resampled stack.

Table 8. Volume calculation of DICOM and Resampled stack.

Stack	No. of Voxels	Voxel Size	Volume (mm ³)
DICOM	21623	1.0089032	21,815.5
Resampled	26911	0.9998	26,905.6

Tumor volume is calculated for the DICOM grid using the physical spacing metadata available in the DICOM header. The inter-slice resolution of the considered patient study is coarse, as the slice thickness is 5 mm, which is considerably higher than the in-plane pixel size, i.e., 0.4492 mm. This anisotropic characteristic results in appalling issues for modeling 3D and image analysis. Thus resampling is often considered as a vital step to transform DICOM stack to an isotropic stack. In the resampled stack, the accuracy of integrating the contours of individual slices not degraded; also, it interpolates the z dimension with lower resolution and in-plane dimensions with higher resolution.

Figure 14 shows the 3D models of DICOM and resampled grid for the patient study. The three anatomical planes are used, and their dimensions are set in mm. For the DICOM grid in Figure 14a, it is observed that the dimensions [X × Y × Z] are set as [512 × 512 × 22]. Similarly, the resampled grid in Figure 14b the dimensions are viewed as [230 × 230 × 110]. The model permits to visualize the object interactively in all the three directions specified.

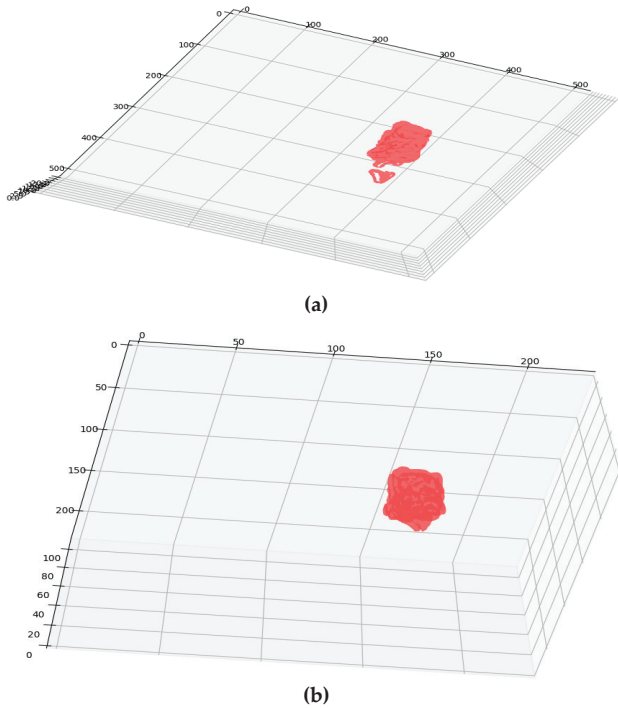


Figure 14. (a) DICOM Grid; (b) Resampled Grid.

From Figure 14a,b, it is clear that the resampled grid offers a smoother surface than the DICOM grid. Resampled grid offers a smoother iso-surface and better 3D visualization.

The proposed work had been validated against various modalities of the BRATS dataset and clinical slices. The performance progression is carried out at each stage of the suggested segmentation procedure. The fuzzy clustering technique had given prominent results in the enhancement phase that aids in effective extraction in post-processing stages. The proposed work had considered two to nine classes (k) that were applied on each slice of the patient under study for ascertaining the most prominent k that could yield the best segmentation. The silhouette score is taken as validation metric results in the optimal enhancement of slices since it considers the $k_{best,i}$ measure for making up the number of required classes. This validated clustering process helps in minimizing the loss of tumor intensities over the patient study. Also, a comparative segmentation analysis had been carried out against Chan-Vese and watershed algorithms for ensuring the segmentation quality of FC. To overcome the computational complexity, the proposed work had considered $k = 9$ as the upper limit for the number of clusters. For DRLS post-processing, imparting single well potential function and Gaussian kernel value as 1.5 had yielded better extraction of tumor part than RG and MCW techniques. In the future, the proposed procedure can be pondered on brain slices containing diffused boundaries and other image modalities in addition to magnetic resonance angiograms (MRA).

4. Conclusions

In this work, a hybrid procedure is implemented, which uses fuzzy clustering with silhouette analysis followed by MCW, RG, and DRLS procedures. Moreover, this proposed method applied to the entire slices of abnormal patient studies obtained from the BRATS challenge and the Proscans Diagnostics Centre. This investigation delivered better segmentation of the regions where the concentration of tumor was high. The best-segmented objects are obtained using clustering techniques which are further evaluated by silhouette metrics. The tumor objects from the enhanced slices are segmented based on MCW/RG/DRLS techniques. The quantification results of the mined anomalies ensure the progression of counterpart tumors at different treatment stages. The clinical significance of the proposed hybrid approach gives a better prognosis identification against the ground truth. The use of python open source technologies in implementing the work can visualize, analyze and interact with the slice data claim to be cost-effective. Hence, the proposed framework on MR DICOM slices requires less user intervention in extracting tumor heterogeneity from typical brain structures. Quantification and 3D modeling procedure help in finding a spatial identity and tumor concentration. By knowing the size, shape and spatial location of the tumor, the process of treating the tumor might be improved. The future work could include the implementation of advanced artificial intelligence methodologies for early, efficient, and real-time diagnosis of malignant brain tumors [58–65].

Supplementary Materials: The video abstract can be found at the following link: <https://drive.google.com/file/d/1ddr0DxPNP1cX7aMC-dvSx12sQJ4fuH59/view?ts=5e452180>. Video: An Efficient Hybrid Fuzzy-Clustering Driven 3D-Modeling.

Author Contributions: Conceptualization, S.K., D.S.; methodology, S.K., D.S., D.R.V.P.M.; software, S.K.; validation, K.S., D.N.K.J., D.G.R.; formal analysis, S.K., D.S., D.R.V.P.M.; investigation, S.K., D.S., D.R.V.P.M.; resources, K.S.; data curation, S.K., K.S.; writing—original draft preparation, S.K.; writing—review and editing, D.S., D.R.V.P.M., K.S., D.N.K.J., D.G.R., A.I.; visualization, D.N.K.J., D.G.R.; supervision, K.S., D.N.K.J., and project administration, K.S., D.N.K.J.; funding acquisition, D.N.K.J. All authors have read and agreed to the published version of the manuscript.

Funding: This work was funded, in part, by the Scheme for Promotion of Academic and Research Collaboration (SPARC), Ministry of Human Resource Development, India under the SPARC/2018-2019/P145/SL, in part, by the framework of Competitiveness Enhancement Program of the National Research Tomsk Polytechnic University, Russia in part, and in part, by the International cooperation project of Sri Lanka Technological Campus, Sri Lanka and Tomsk Polytechnic University, Russia, No. RRSG/19/5008.

Acknowledgments: The authors would like to acknowledge the support granted by Proscans Diagnostics Centre, the leading and reputed Pathology Lab network in Chennai, Tamilnadu, India, for providing real clinical images of the brain MRI.

Conflicts of Interest: The authors declare that they have no conflict of interest.

Ethical Approval: This article follows the ethical standards of 1964 Helsinki declaration with its future amendments.

References

1. Karaa, W.B. *Biomedical Image Analysis and Mining Techniques for Improved Health Outcomes*; IGI Global: Hershey, USA, 2015. [\[CrossRef\]](#)
2. El-Dahshan, E.S.; Mohsen, H.M.; Revett, K.; Salem, A.B.M. Computer-aided diagnosis of human brain tumor through MRI: A survey and a new algorithm. *Expert Syst. Appl.* **2014**, *41*, 5526–5545. [\[CrossRef\]](#)
3. Chyzhyk, D.; Savio, A.; Graña, M. Evolutionary ELM wrapper feature selection for Alzheimer’s disease CAD on anatomical brain MRI. *Neurocomputing* **2014**, *128*, 73–80. [\[CrossRef\]](#)
4. Virmani, J.; Dey, N.; Kumar, V. PCA-PNN, and PCA-SVM based CAD systems for breast density classification. In *Applications of Intelligent Optimization in Biology and Medicine*; Springer: Berlin/Heidelberg, Germany, 2016; pp. 159–180.
5. Bahadure, N.B.; Ray, A.K.; Thethi, H.P. Image analysis for MRI based brain tumor detection and feature extraction using biologically inspired BWT and SVM. *Int. J. Biomed. Imag.* **2017**, *2017*. [\[CrossRef\]](#)
6. Fujita, H.; Uchiyama, Y.; Nakagawa, T.; Fukuokab, D.; Hatanakac, Y.; Hara, T.; Lee, G.N.; Hayashi, Y.; Ikeda, Y.; Gaoa, X.; et al. Computer-aided diagnosis: The emerging of three CAD systems induced by Japanese health care needs. *Comput. Methods Progr. Biomed.* **2008**, *92*, 238–248. [\[CrossRef\]](#)
7. Marshkole, N.; Singh, B.K.; Thoke, A.S. Texture and shape-based classification of brain tumors using linear vector quantization. *Int. J. Comput. Appl.* **2011**, *30*, 21–23.
8. Arimura, H.; Tokunaga, C.; Yamashita, Y.; Kuwazuru, J. Magnetic resonance image analysis for brain CAD systems with machine learning. In *Machine Learning in Computer-Aided Diagnosis: Medical Imaging Intelligence and Analysis*; IGI Global: Hershey, USA, 2012; pp. 258–296. [\[CrossRef\]](#)
9. Bidgood Jr, W.D.; Horii, S.C.; Prior, F.W.; Van Syckle, D.E. Understanding and using DICOM, the data interchange standard for biomedical imaging. *J. Am. Med. Inf. Assoc.* **1997**, *4*, 199–212. [\[CrossRef\]](#)
10. Herrmann, M.D.; Clunie, D.A.; Fedorov, A.; Doyle, S.W.; Pieper, S.; Klepeis, V.; Le, L.P.; Mutter, G.L.; Milstone, D.S.; Schultz, T.J.; et al. Implementing the DICOM standard for digital pathology. *J. Pathol. Inform.* **2018**, *9*, 1–18. [\[CrossRef\]](#)
11. Suresh, K.; Sakthi, U. Robust multi-thresholding in noisy grayscale images using Otsu’s function and harmony search optimization algorithm. In *Advances in Electronics, Communication and Computing*; Springer: Singapore, 2018. [\[CrossRef\]](#)
12. Hartigan, J.A.; Wong, M.A. Algorithm AS 136: A k-means clustering algorithm. *J. R. Stat. Soc. Ser. C* **1979**, *28*, 100–108. [\[CrossRef\]](#)
13. Dhanachandra, N.; Manglem, K.; Chanu, Y.J. Image segmentation using K-means clustering algorithm and subtractive clustering algorithm. *Proc. Comput. Sci.* **2015**, *54*, 764–771. [\[CrossRef\]](#)
14. Abdel-Maksoud, E.; Elmogy, M.; Al-Awadi, R. Brain tumor segmentation based on a hybrid clustering technique. *Egypt. Inf. J.* **2015**, *16*, 71–81. [\[CrossRef\]](#)
15. Kim, K.B.; Song, Y.S.; Park, H.J.; Song, D.H.; Choi, B.K. A fuzzy C-means quantization based automatic extraction of rotator cuff tendon tears from ultrasound images. *J. Intell. Fuzzy Syst.* **2018**, *35*, 149–158. [\[CrossRef\]](#)
16. Dehariya, V.K.; Shrivastava, S.K.; Jain, R.C. Clustering of image data set using k-means and fuzzy k-means algorithms. In *Proceedings of the 2010 International Conference on Computational Intelligence and Communication Networks*, Bhopal, India, 26–28 November 2010; pp. 386–391. [\[CrossRef\]](#)
17. Gasch, A.P.; Eisen, M.B. Exploring the conditional coregulation of yeast gene expression through fuzzy k-means clustering. *Genome Biol.* **2002**, *3*, research0059-1. [\[CrossRef\]](#) [\[PubMed\]](#)
18. Rajinikanth, V.; Raja, N.S.M.; Kamalanand, K. Firefly algorithm assisted segmentation of tumor from brain MRI using Tsallis function and Markov random field. *J. Control Eng. Appl. Inf.* **2017**, *19*, 97–106.
19. Raja, N.S.M.; Lakshmi, P.R.V.; Gunasekaran, K.P. Firefly algorithm-assisted segmentation of brain regions using tsallis entropy and Markov random field. In *Innovations in Electronics and Communication Engineering*; Springer: Singapore, 2018; pp. 229–237.
20. Gath, I.; Geva, A.B. Unsupervised optimal fuzzy clustering. *IEEE Trans. Pattern Anal. Mach. Intell.* **1989**, *515*, 87–100. [\[CrossRef\]](#)
21. Llet, R.; Ortiz, M.C.; Sarabia, L.A.; Sánchez, M.S. Selecting variables for k-means cluster analysis by using a genetic algorithm that optimises the silhouettes. *Anal. Chim. Acta* **2004**, *515*, 87–100. [\[CrossRef\]](#)

22. Muca, M.; Kutrolli, G.; Kutrolli, M. A proposed algorithm for determining the optimal number of clusters. *Eur. Sci. J.* **2015**, *11*, 36.
23. Zeng, Y.Z.; Liao, S.H.; Tang, P.; Zhao, Y.Q.; Liao, M.; Chen, Y.; Liang, Y.X. Automatic liver vessel segmentation using 3D region growing and hybrid active contour model. *Comput. Biol. Med.* **2018**, *97*, 63–73. [\[CrossRef\]](#)
24. Koulountzios, P.I.; Zervakis, M.E.; Karakitsios, P.L.; Stavroulakis, G.E. A semi-automatic algorithm for reconstruction and NURBS surface generation of thoracic aorta. In Proceedings of the 2017 IEEE International Conference on Imaging Systems and Techniques (IST), Beijing, China, 20 October 2017; pp. 1–6. [\[CrossRef\]](#)
25. Nekooimehr, I.; Lai-Yuen, S.; Bao, P.; Weitzenfeld, A.; Hart, S. Automated contour tracking and trajectory classification of pelvic organs on dynamic MRI. *J. Med. Image.* **2018**, *5*, 014008. [\[CrossRef\]](#)
26. Wang, H.; Ahmed, S.N.; Mandal, M. Computer-aided diagnosis of cavernous malformations in brain MR images. *Comput. Med. Image Gr.* **2018**, *66*, 115–123. [\[CrossRef\]](#)
27. Arbelaez, P.; Maire, M.; Fowlkes, C.; Malik, J. Contour detection and hierarchical image segmentation. *IEEE Trans. Pattern Anal. Mach. Intell.* **2010**, *33*, 898–916. [\[CrossRef\]](#)
28. Essadike, A.; Ouabida, E.; Bouzid, A. Brain tumor segmentation with Vander Lugtcorrelator based active contour. *Comput. Meth. Prog. Biomed.* **2018**, *160*, 103–117. [\[CrossRef\]](#) [\[PubMed\]](#)
29. Hemalatha, S.; Anuncia, S.M. A computational model for texture analysis in images with fractional differential filter for texture detection. *Int. J. Ambient Comput. Intell.* **2016**, *7*, 93–113. [\[CrossRef\]](#)
30. Hu, S.; Wang, X.; Zhu, M.; Hao, G.; Yao, C.; Hu, C.-H. Differentiation of High-grade Gliomas from Brain Metastases Using Tissue Similarity Maps (TSMs) Based Relative Cerebral Blood Volume Values. *Curr. Med. Image Rev.* **2018**, *14*, 594–598. [\[CrossRef\]](#)
31. Ali, S.M.; Abood, L.K.; Abdoon, R.S. Brain tumor extraction in MRI images using clustering and morphological operations techniques. *Int. J. Geogr. Inf. Syst. Appl. Remote Sens.* **2013**, *4*, 12–25.
32. Deng, L.; Huang, H.; Yuan, J.; Tang, X. Automatic segmentation of corneal ulcer area based on ocular staining images. In Proceedings of the Medical Imaging 2018: Biomedical Applications in Molecular, Structural, and Functional Imaging; International Society for Optics and Photonics: Houston, TX, USA, 2018. [\[CrossRef\]](#)
33. Dey, N.; Rajinikanth, V.; Ashour, A.S.; Tavares, J.M.R. Social group optimization supported segmentation and evaluation of skin melanoma images. Symmetry. *Int. J. Geogr. Inf. Syst. Appl. Remote Sens.* **2013**, *4*, 12–25.
34. Chang, C.-Y.; Srinivasan, K.; Chen, M.-C.; Chen, S.-J. SVM-Enabled Intelligent Genetic Algorithmic Model for Realizing Efficient Universal Feature Selection in Breast Cyst Image Acquired via Ultrasound Sensing Systems. *Sensors* **2020**, *20*, 432. [\[CrossRef\]](#)
35. Baghaie, A.; Yu, Z. An optimization method for slice interpolation of medical images. *arXiv* **2014**, arXiv:1402.0936.
36. Chenevert, T.L.; Malyarenko, D.I.; Newitt, D.; Li, X.; Jayatilake, M.; Tudorica, A.; Fedorov, A.; Kikinis, R.; Liu, T.T.; Muzi, M.; et al. Errors in quantitative image analysis due to platform-dependent image scaling. *Trans. Oncol.* **2014**, *7*, 65–71. [\[CrossRef\]](#)
37. Rousseeuw, P.J.J. A graphical aid to the interpretation and validation of cluster analysis. *J. Comput. Appl. Math.* **1987**, *20*, 53–65. [\[CrossRef\]](#)
38. Del Re, E.C.; Gao, Y.; Eckbo, R.; Petryshen, T.L.; Blokland, G.A.M.; Seidman, L.J.; Konishi, J.; Goldstein, J.M.; McCarley, R.W.; Shenton, M.E.; et al. A New MRI Masking Technique Based on Multi-Atlas Brain Segmentation in Controls and Schizophrenia: A Rapid and Viable Alternative to Manual Masking. *J. Neuroimaging* **2016**, *26*, 28–36. [\[CrossRef\]](#)
39. Russakoff, D.B.; Tomasi, C.; Rohlfing, T.; Maurer, C.R. Image similarity using mutual information of regions. In Proceedings of the European Conference on Computer Vision, Prague, Czech Republic, 11 May 2004; pp. 596–607. [\[CrossRef\]](#)
40. Chaddad, A.; Tanougast, C. Quantitative evaluation of robust skull stripping and tumor detection applied to axial MR images. *Brain Inf.* **2016**, *3*, 53–61. [\[CrossRef\]](#) [\[PubMed\]](#)
41. Rajinikanth, V.; Satapathy, S.C.; Fernandes, S.L.; Nachiappan, S. Entropy-based segmentation of tumor from brain MR images—A study with teaching learning-based optimization. *Pattern Recognit. Lett.* **2016**, *94*, 87–94. [\[CrossRef\]](#)
42. Thanaraj, P.; Parvathavarthini, B. Multichannel interictal spike activity detection using time–frequency entropy measure. *Australas. Phys. Eng. Sci. Med.* **2017**, *40*, 413–425. [\[CrossRef\]](#) [\[PubMed\]](#)

43. Rajinikanth, V.; Dey, N.; Satapathy, S.C.; Ashour, A.S. An approach to examine magnetic resonance angiography based on Tsallis entropy and deformable snake model. *Future Gener. Future Comput. Syst.* **2018**, *85*, 160–172. [\[CrossRef\]](#)
44. Roopini, I.T.; Vasanthi, M.; Rajinikanth, V.; Rekha, M.; Sangeetha, M. Segmentation of tumour from brain MRI using fuzzy entropy and distance regularised level set. In Proceedings of the Computational Signal Processing and Analysis, Singapore, 3 April 2018; pp. 297–304.
45. Rajinikanth, V.; Satapathy, S.C.; Dey, N.; Vijayarajan, R. DWT-PCA Image fusion technique to improve segmentation accuracy in brain tumour analysis. In *Microelectronics, Electromagnetics and Telecommunications*; Springer: Singapore, 2018; pp. 453–462. Available online: https://link.springer.com/chapter/10.1007/978-981-10-7329-8_46 (accessed on 5 February 2020). [\[CrossRef\]](#)
46. Krishnan, P.T.; Balasubramanian, P.; Krishnan, C. Segmentation of brain regions by integrating meta heuristic multilevel threshold with markov random field. *Curr. Med. Imaging* **2016**, *12*, 4–12. [\[CrossRef\]](#)
47. Chen, Y.H.; Chang, C.C.; Lin, C.C.; Hsu, C.Y. Content-based color image retrieval using block truncation coding based on binary ant colony optimization. *Symmetry* **2019**, *11*, 21. [\[CrossRef\]](#)
48. Kalaiselvi, T.; Selvi, S.K. Investigation of Image Processing Techniques in MRI Based Medical Image Analysis Methods and Validation Metrics for Brain Tumor. *Curr. Med. Image Rev.* **2018**, *14*, 489–505. [\[CrossRef\]](#)
49. Rajinikanth, V.; Thanaraj, K.P.; Satapathy, S.C.; Fernandes, S.L.; Dey, N. Shannon's entropy and watershed algorithm based technique to inspect ischemic stroke wound. In *Smart Intelligent Computing and Applications*; Springer: Singapore, 2019; pp. 23–31.
50. Suresh, K.; Sakthi, U. Object Tracking based 3d Modelling and Quantification of Abnormal Contours in Brain MRI DICOM Study. *J. Eng. Sci. Technol.* **2019**, *14*, 2098–2115.
51. Shanthakumar, P.; Ganesh Kumar, P. Computer aided brain tumor detection system using watershed segmentation techniques. *Int. J. Image Syst. Technol.* **2015**, *25*, 297–301. [\[CrossRef\]](#)
52. Chan, T.F.; Vese, L.A. Active contours without edges. *IEEE Trans. Image Proc.* **2001**, *10*, 266–277. [\[CrossRef\]](#)
53. Memon, F.; Unar, M.A.; Memon, S. Image quality assessment for performance evaluation of focus measure operators. *arXiv* **2016**, arXiv:1604.00546.
54. Moga, A.N.; Gabbouj, M. Parallel marker-based image segmentation with watershed transformation. *J. Parallel Distrib. Comput.* **1998**, *51*, 27–45. [\[CrossRef\]](#)
55. Suresh, K.; Sakthi, U. A soft-computing based hybrid tool to extract the tumour section from brain MRI. *Multimed. Tools Appl.* **2019**, 1–5. [\[CrossRef\]](#)
56. Raja, N.S.; Fernandes, S.L.; Dey, N.; Satapathy, S.C.; Rajinikanth, V. Contrast enhanced medical MRI evaluation using Tsallis entropy and region growing segmentation. *J. Ambient Intel. Hum. Comput.* **2018**, 1–12. [\[CrossRef\]](#)
57. Chang, C.Y.; Srinivasan, K.; Hu, H.Y.; Tsai, Y.S.; Sharma, V.; Agarwal, P. SFFS-SVM based prostate carcinoma diagnosis in DCE-MRI via ACM segmentation. *Multidim. Syst. Sign. Process.* **2019**, 1–22. [\[CrossRef\]](#)
58. Kathiravan, S.; Kanakaraj, J. A Review of Magnetic Resonance Imaging Techniques. *Smart Comput. Rev.* **2013**, *3*, 358–366. [\[CrossRef\]](#)
59. Hua, K.; Dai, B.; Srinivasan, K.; Hsu, Y.H.; Sharma, V. A hybrid NSCT domain image watermarking scheme. *J. Image Video Proc.* **2017**, 2017, 10. [\[CrossRef\]](#)
60. Srinivasan, K.; Sharma, V.; Jayakody, D.N.K.; Vincent, D.R. D-ConvNet: Deep learning model for enhancement of brain MR images. In Proceedings of the Basic & Clinical Pharmacology & Toxicology, Hoboken, NJ, USA, 23–24 December 2018; Volume 124, pp. 3–4. [\[CrossRef\]](#)
61. Srinivasan, K.; Ankur, A.; Sharma, A. Super-resolution of Magnetic Resonance Images using deep Convolutional Neural Networks. In Proceedings of the 2017 IEEE International Conference on Consumer Electronics—Taiwan (ICCE-TW), Taipei, China, 12–14 June 2017; pp. 41–42. [\[CrossRef\]](#)
62. Kathiravan, S.; Kanakaraj, J. A Review on Potential Issues and Challenges in MR Imaging. *Sci. World J.* **2013**, *10*. [\[CrossRef\]](#)
63. Srinivasan, K.; Kanakaraj, J. A Study on Super-Resolution Image Reconstruction Techniques. *Comput. Eng. Intell. Syst.* **2011**, *2*, 222–227.

64. Srinivasan, K.; Kanakaraj, J. An Overview of SR Techniques Applied to Images, Videos and Magnetic Resonance Images. *Smart Comput. Rev.* **2014**, *4*, 181–201. [[CrossRef](#)]
65. Hua, K.-L.; Trang, H.T.; Srinivasan, K.; Chen, Y.-Y.; Chen, C.-H.; Sharma, V.; Zomaya, A.Y. Reduction of Artefacts in JPEG-XR Compressed Images. *Sensors* **2019**, *19*, 1214. [[CrossRef](#)] [[PubMed](#)]



© 2020 by the authors. Licensee MDPI, Basel, Switzerland. This article is an open access article distributed under the terms and conditions of the Creative Commons Attribution (CC BY) license (<http://creativecommons.org/licenses/by/4.0/>).

Article

Automated Volume Status Assessment Using Inferior Vena Cava Pulsatility

Luca Mesin ^{1,*}, Silvestro Roatta ², Paolo Pasquero ³ and Massimo Porta ³

¹ Mathematical Biology and Physiology, Department of Electronics and Telecommunications, Politecnico di Torino, 10129 Turin, Italy

² Integrative Physiology Lab, Department of Neuroscience, Università di Torino, 10125 Turin, Italy; silvestro.roatta@unito.it

³ Department of Medical Sciences, Università di Torino, 10126 Turin, Italy; pasquerop@gmail.com (P.P.); massimo.porta@unito.it (M.P.)

* Correspondence: luca.mesin@polito.it; Tel.: +39-011-090-4085

Received: 14 September 2020; Accepted: 7 October 2020; Published: 13 October 2020

Abstract: Assessment of volume status is important to correctly plan the treatment of patients admitted and managed by cardiology, emergency and internal medicine departments. Non-invasive assessment of volume status by echography of the inferior vena cava (IVC) is a promising possibility, but its clinical use is limited by poor reproducibility of current standard procedures. We have developed new algorithms to extract reliable information from non-invasive IVC monitoring by ultrasound (US) imaging. Both long and short axis US B-mode video-clips were taken from 50 patients, in either hypo-, eu-, or hyper-volemic conditions. The video-clips were processed to extract static and dynamic indexes characterizing the IVC behaviour. Different binary tree models (BTM) were developed to identify patient conditions on the basis of those indexes. The best classifier was a BTM using IVC pulsatility indexes as input features. Its accuracy (78.0% when tested with a leave-one-out approach) is superior to that achieved using indexes measured by the standard clinical method from M-mode US recordings. These results were obtained with patients in conditions of normal respiratory function and cardiac rhythm. Further studies are necessary to extend this approach to patients with more complex cardio-respiratory conditions.

Keywords: inferior vena cava; ultrasound imaging; binary tree model; pulsatility; fluid volume assessment

1. Introduction

The intravascular volume status (i.e., the extent of vascular filling) is a relevant cardiovascular parameter related to the cardiac preload (i.e., the stretch of cardiac tissue in relaxed conditions), which in turn affects cardiac output and arterial blood pressure. Its assessment in critically ill patients is essential to establish and carefully balance the appropriate fluid therapy, whereby fluid supplementation may favor cardiac efficiency, but also increase the rate of complications and mortality [1–3]. Various pathological conditions are characterized by alteration of the volume status, e.g., heart failure causes overload while dehydration leads to volume depletion.

The non invasive evaluation of the volume status is very important, as it allows to inspect a patient in emergency conditions or during the follow-up. An approximate assessment of the volemic condition can be obtained from US imaging of the IVC [4,5]. In fact, the pulsatility of the IVC was found to correlate with the intravascular fluid volume [6]. Moreover, it can be useful for the non-invasive estimation of the central venous pressure [7–9].

However, this non-invasive method has shown limitations [10,11]. Important problems are due to the lack of standardization [12] and to the subjectivity of the measurement [13]. Indeed, both B-mode and M-mode US scans have been used, followed by a subjective identification of the IVC maximal and minimal diameters [6,14]. Specifically, IVC pulsatility can be expressed in terms of the caval index (CI), defined as the variation of the vessel diameter during a respiratory cycle relative to the maximum diameter: minimum and maximum diameters are measured by the operator from a B-mode video or an M-mode trace considering inspiration and expiration, respectively. This clinical approach is not standardized [12,15] (e.g., either long [16] or short axis [17] visualizations are used), and is operator-dependent [13] and prone to measurement errors, e.g., due to movements [18] and non-uniform pulsatility of IVC [15]. In particular, the M-mode registration allows to visualize a section of the vein over time at high frequency along a fixed direction in space [19]. As the IVC moves during respiration, the M-mode approach fails to constantly refer to the same section of the vein. On the other hand, measuring diameters from a B-mode video requires that the operator chooses the frames corresponding to the end of inspiration and expiration, in addition to selecting the sections along which to estimate the diameters (which could be different, if the operator does not compensate for IVC movement).

Moreover, IVC pulsatility may vary considerably in different portions of the vein [15,20], so that a single measurement taken by a manual approach provides limited information.

Some confounding factors have also been documented in case of specific pathologies, e.g., to the respiratory system [21,22] or the heart [23,24]. Indeed, breathing and heartbeats provide the main stimulations affecting IVC pulsatility. Separating the effects of the two contributions could possibly help to counteract these limitations [13,25].

A further problem consists in the shape of the IVC: in different sections along the longitudinal view, the IVC can exhibit very different diameters, as in the case of a saber profile [15,26], and different pulsilities [20]; the IVC cross-section can be irregular, much different from a circle or an ellipsoid (especially in the case of hypo-volemia), with a large variation of pulsatility in different directions [27,28]. Thus, investigating IVC both in long and short axis views and averaging across different sections or directions could be important to better characterize the vessel and its respirophasic dynamics.

We have carried out a series of studies trying to overcome some of the limitations of the US assessment of IVC. Specifically, we have developed an automated method to track the movements and estimate the borders of the IVC from US video-clips [19,20,28,29]. Data derived from both longitudinal (long axis) and transverse (short axis) sections of the vessel can be processed. The algorithms extract information from either a whole tract of longitudinal section of the vein or a transverse section, respectively. This way, the overall pulsatility can be estimated. Moreover, the border of the vein is found for each frame of the video-clip, so that the vessel pulsations can be investigated over time, obtaining time series which can be processed to estimate further indexes characterizing pulsatility, e.g., induced by either respiration or cardiac stimulation only. Preliminary results indicate that IVC average size and global pulsatility and its respiratory and cardiac components estimated in long axis are strongly related to the right atrial pressure (in contrast with size and pulsatility estimated by standard clinical approaches [30]) and are useful for its non-invasive estimation [25,31].

However, beyond these promising correlations, there is still no stable criterion capable of recognizing pathological problems in the volume status. With this study, we face this aspect and try to propose a classification method based on an automated processing. Specifically, US B-mode video-clips of IVC from long and short axis have been acquired from patients with different volume status. They have been processed, tracking the movements and estimating the border of the vein. Then, indexes characterizing IVC size and pulsatility have been automatically extracted and used to build a classifier able to discriminate patients in either hypo-, eu-, or hyper-volemic conditions.

2. Methods

2.1. US Video-Clip Processing

The physical dimension of a pixel was determined for each video-clip as a preliminary step, by scanning automatically a graduated length scale present in the frames. Then, the user selected some parameters (e.g., concerning the portion of frame to be processed, points to be tracked, etc.) needed by two algorithms (implemented in MATLAB R2018a, The Mathworks) that processed the B-mode US video-clips of the IVC in either long or short axis (notice that, as a preliminary interaction with the user is needed to process the US videos, we refer to our processing algorithms as semi-automated). Figure 1 shows an example of IVC border automated delineation obtained by those algorithms, described below. Once obtained the IVC borders in either of the two views, the mean diameter and pulsatility indexes (defined below) were estimated.

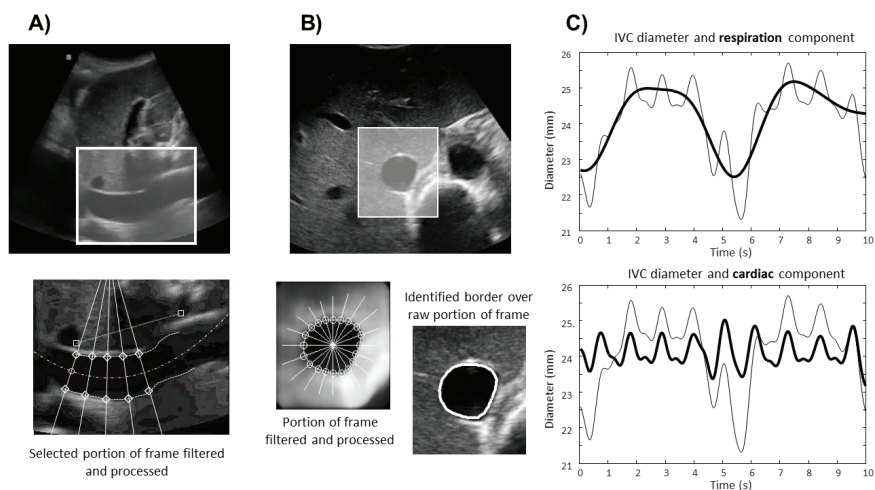


Figure 1. (A) Example of single frame of a video-clip of the IVC in long axis and result of processing (5 equidistant sections in direction orthogonal to the IVC midline are considered). (B) Example of frame in short axis and processing (median filter is applied on the bottom left figure, different rays are originated from the centre of the vein and their intersections with the border of the vessel are computed; estimated IVC border indicated in the bottom right image). (C) Representative example of IVC diameter over time (the average of the diameters of the case shown in A is considered, only for representation purposes): from the time series, respiratory and cardiac components (the latter added to the average diameter, for clearer representation) are extracted by specific filters.

2.1.1. Identification of IVC Borders in Long Axis

The algorithm proposed in [20] (and already applied in [13,25,31]) was used. In the first frame of the clip, the user located the vein and the region of interest, indicating two reference points to be tracked to compensate for IVC movements and deformations, the leftmost and rightmost lines to be considered and the location of the borders of the vein in the leftmost line. In optimal conditions, the available tract was between the confluence of the hepatic veins into the IVC and the caudate lobe of the liver. Each frame was first pre-processed with a 2D median filter (neighborhoods of 9×9 pixels). Then, the software uniformly

distributed 21 lines in the region of interest and identified the borders of the vein along these lines (as a jump of the US intensity along them). For each subsequent frame, the location and direction of those lines were updated based on the estimated movements of the reference points from the previous one.

Once obtained the superior and inferior borders of the vein, the software computed the IVC midline and distributed uniformly 5 points along it. For our specific application, the extension of the midline was considered only from the 20% to the 80% of its length, thus excluding the edges. Sections orthogonal to the IVC midline passing from each of these 5 points were considered and the IVC pulsatility was estimated for each of them.

2.1.2. Identification of IVC Borders in Short Axis

The algorithm proposed in [28] (and already used in [29]) was employed. The user was asked to indicate the centre of the IVC and to draw a rectangle enclosing it in the first frame of the video-clip. Subsequent frames were cropped in a rectangular region with the same dimension, centered on the IVC estimated on the previous frame.

The image was converted in gray-scale, contrast enhanced using histogram equalization and processed with a 2D median filter (neighborhoods of 11×11 pixels). The outline of the vein was then estimated by the algorithm. Twenty rays were defined, originating from the centre of the considered rectangular portion of image and sampling uniformly the directions around it. For each ray, the intensity of the image along it was estimated by cubic interpolation. The border of the vein was identified as an abrupt increase of the intensity (from the lumen to the outside tissues).

Once the 20 border points were found, their coordinates were low pass filtered (Butterworth non-causal, zero-phase IIR filter of order 4 with cut-off at 0.3) to get a smooth boundary of the vein. Furthermore, the maximum variation of the length of a ray was imposed to be 5 pixels; the rays which overcame such a threshold were removed and substituted by a quadratic interpolation of the 4 closest neighboring border points.

2.1.3. IVC Indexes

The mean diameter was estimated averaging both across different sections (i.e., 5 sections in long axis and 10 diameters corresponding to the 20 rays in short axis) and time (i.e., considering the frames of the video-clips).

Pulsatility was measured in terms of the CI

$$CI = \frac{\max_t (D(t)) - \min_t (D(t))}{\max_t (D(t))} \quad (1)$$

where D indicates the dimension over the time variable t of IVC, expressed either as diameter or equivalent diameter (proportional to the square root of the area [28]), in the long and short axis, respectively, and max/min indicate local extrema. Local maxima and minima were computed for each respiratory cycle. A CI accounting for the overall pulsatility was obtained by averaging the estimations across different respiratory cycles and different sections (the latter, only in the case of the long axis approach).

Additional indexes were also estimated by decomposing the time series reflecting IVC pulsations into low and high frequency components (below 0.4 Hz and above 0.8 Hz, respectively), assumed to reflect the stimulations induced by either respiration or heartbeats, respectively (both filters were 4th order Butterworth, used twice, once with time reversed, to remove phase distortion and delay). From these filtered time series, applying again the definition of CI (1) on local maxima and minima, the respiratory caval index (RCI) and the cardiac caval index (CCI) were obtained. Stable estimations of both indexes were

computed by averaging across either respiratory cycles or heartbeats (and on the 5 sections, in the case of the long axis).

An example of time series extracted from a video-clip is given in Figure 1C.

IVC was also investigated by standard manual measurements, in both long and short axis, in M-mode. Stable estimations of the minimum and maximum IVC diameter were obtained by averaging across more measurements (up to 3). Then, the maximum and minimum diameters were used to compute the CI and the average IVC diameter (defined as the mean of the two diameters).

2.2. Experimental Data

Inclusion criteria were the presence of pathological conditions in the Emergency Department and in the Department of Medicine resulting in overload (heart failure) or volume depletion (dehydration or moderate bleeding). As a control group, patients without the previous conditions were selected. Exclusion criteria were chronic obstructive pulmonary disease, pulmonary hypertension, interstitial disease or thromboembolism, tension pneumothorax, cirrhosis and/or ascitic effusion, serum creatinine >3 mg/dL, constrictive pericarditis and cardiac tamponade. Fifty patients were included in the study. They were selected from a database of 69 patients (Table 1). On the basis of clinical considerations (based upon physical examination, laboratory data and imaging), each patient was associated to one of the following classes:

1. hypo-volemic condition (20 subjects);
2. eu-volemic condition (24 subjects);
3. hyper-volemic condition (25 subjects).

US B-mode video-clips of about 15 s were recorded bedside in spontaneous breathing, with subxifoideal approach, using a MyLab Seven system (Esaote, Genova, Italy; frame rate 30 Hz, 256 gray levels) equipped with a convex 2–5 MHz probe. M-mode scans were also recorded to allow for standard manual measurements.

According to the Declaration of Helsinki, subjects provided written informed consent for the collection of data and subsequent analysis. The study was approved by the local Ethics Committee.

The data included here were only those for which both video-clips, recorded along either long or short axis, could be reliably processed. They were 20 from patients in overload, 19 controls and 11 patients with volume depletion (notice that video-clips of patients with volume depletion are more difficult to be processed, due to the small dimension of the IVC, which could even collapse in some frames, hindering proper processing).

Figure 2 shows examples of patients in the 3 classes.

Table 1. Number of patients included in different groups (with indication of the entire database and of the patients for which successful processing of both long and short axis ultrasound videos was achieved).

	Hypo-Volemic	Eu-Volemic	Hyper-Volemic
Database	20	24	25
Successful processing	11	19	20
Rate of successful processing	55.0%	79.2%	80.0%

2.3. Automated Identification of the Volemic Status

Three different classification approaches were fit to our dataset, as a preliminary step: the error-correcting output codes (ECOC) model, using support vector machines (SVM [32]) for binary one-to-one classifications [33,34]; the Naive Bayes classifier (estimating data distributions using smoothed densities with normal kernel) [35]; the BTM [35]. For each approach, different models were fit to our data,

considering all possible combinations of input features (detailed below). The performances of different classifiers were compared in terms of a 10-fold cross-validation test, which allowed to select the best input features and classification approach. Then, the selected classifier was tested by a leave-one-out approach and, finally, trained on the entire dataset, to provide an ultimate prediction model. In the following, we will focus only on the BTM, as best results were obtained using this approach.

Different BTMs were fit to our multi-class classification problem (including 3 classes), selecting the simplest one (i.e., with minimum dimension) with best performances. A BTM iteratively splits the dataset in two groups, after comparing an index with a threshold (Gini's diversity index was used as splitting criterion). Thus, it is built by choosing the optimal number of splittings, the specific index to be considered for each binary separation and selecting the threshold value for each splitting. Different BTMs were developed considering all possible combinations of input indexes (exhaustive search): all possible choices of a single index, all pairs, triplets, ... until using all indexes.

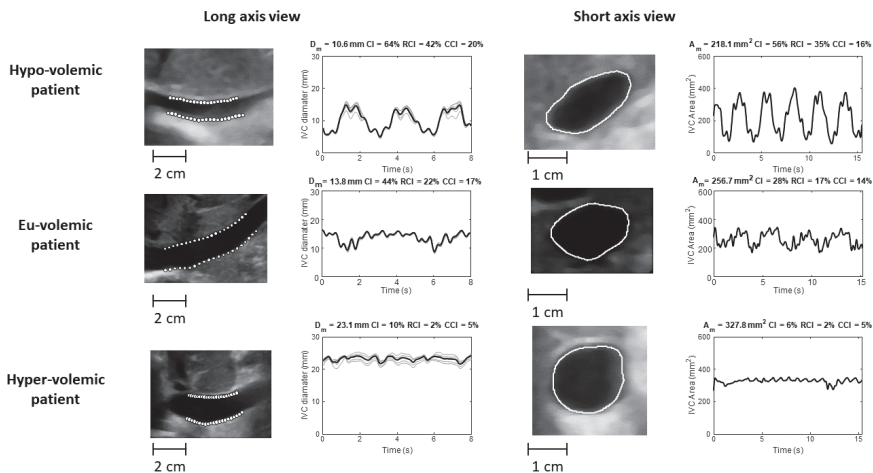


Figure 2. Examples of data from patients in either hypo-, eu- or hyper-volemic conditions. The first frames of the long and short axis scans are shown (left and right, respectively), together with the IVC boundaries identified by the algorithm. Time series are also shown for the diameters in 5 sections of the IVC (in gray, with superimposed the mean diameter in black) and for the IVC area estimated from the long and short axis scans, respectively. In the case of long axis scans, pulsatility indexes were computed as averages of estimations from each of the 5 sections; in the case of short axis scans, they were computed from the equivalent diameter, proportional to the square root of the IVC cross-section area. D_m : mean diameter; A_m : mean area; CI: caval index; RCI: respiratory caval index; CCI: cardiac caval index.

Different sets of indexes were used, considering the possibility of either employing the semi-automated processing or not (so that in the latter case only manual measurements were considered).

The set of indexes obtained by semi-automated video processing was the following:

1. mean diameter of IVC in long axis;
2. CI in long axis;
3. RCI in long axis;
4. CCI in long axis;

5. equivalent diameter of IVC in short axis;
6. CI in short axis;
7. RCI in short axis;
8. CCI in short axis.

The set of indexes obtained by standard manual measurements was the following:

1. diameter of IVC in long axis;
2. CI in long axis;
3. diameter of IVC in short axis;
4. CI in short axis.

For each set of indexes, different BTMs were developed using all possible combinations of features taken from it and the one with highest performance was selected (thus, they were 255 and 15, for the first and second features set, respectively). Specifically, the best categorical predictor split was chosen from all possible combinations of choices. As mentioned above, the models were cross-validated considering 10 folds. The order of the data was random, so that the three categories of patients had a similar representation in each fold (however, they could not be equally represented; this problem is emphasized by the small size of our dataset). The one providing minimum average root mean squared regression error (or loss) on the validation sets was then selected. This specific model was then tested by a leave-one-out approach, to reduce the bias in error estimation (considering our small dataset) [36].

3. Results

Indexes characterizing the IVC were extracted from long and short axis views by either semi-automated processing or manual estimation (performed in M-mode). Then, they were used to classify patients. As using indexes extracted with the automated processing resulted in better performances, figures and tables shown below refer to those data, indicating in the text some performance indexes of the best BTM developed using the set of indexes obtained by standard manual measurements.

Figure 3 shows the BTM selected as the classifier with best performances on our dataset. The shown BTM was trained on the entire dataset, including the best input features selected by the cross-validation test (described in Section 2.3), where minimum loss was obtained (equal to 0.26; the loss of the best classifiers using either ECOC or Naive Bayes models was 0.28).

Two pulsatility indexes are included: CCI in long axis and CI in short axis. The same loss was obtained by other 4 BTMs: the one with minimum number of input features was selected. The CCI in long axis was included in 4 of these BTMs with minimum loss; the CI in short axis was included in 2 of them. Another feature which was often included was the RCI in short axis, which was used in 3 among the 5 BTMs with minimum loss. In the case in which standard manual measurements were employed, the best BTM was unique, it had a loss of 0.28 and included two indexes: IVC diameter estimated in long axis and CI in short axis.

Distributions of the indexes are shown in Figure 4. The mean Fisher ratios (FR, considering all 3 binary comparisons) of the indexes selected by the best BTM between those estimated by semi-automated processing are among the highest. However, they have not the highest FRs: indeed, the best discrimination in terms of average FR is provided by the mean diameter estimated from the long axis view. This indicates that the selected indexes are those that are both informative and not much redundant, allowing a peak in performance of the classifier using them as inputs. Notice also that the FR is an index of linear discrimination, whereas the adopted classifier allows for nonlinear separation.

It is interesting to see that the indexes estimated manually have even higher FRs, indicating a better linear discrimination of the patients. The two indexes with highest FRs are those selected by the best

BTM using only indexes measured manually. However, the semi-automated processing allows to extract additional information: specifically, the two pulsatility indexes RCI and CCI reflect the effect of different stimulations (respiration and heartbeat, respectively). This further information (and specifically that coming from the CCI) allows the BTM from automated processing to get better performances than the one developed on the basis of the set of manually estimated indexes.

The confusion matrix of the best BTM shown in Figure 3 is given in Table 2. Notice that all hypo-volemic patients were correctly identified. A few eu-volemic and hyper-volemic subjects were misclassified. No hyper-volemic patient was confused as hypo-volemic or vice-versa. Common performance indexes are the followings: mean sensitivity 90.0% (86.0% for the BTM built using the manually estimated indexes); mean specificity 95.0% (91.9% with manual indexes); positive predictive value 90.0% (86.2% with manual indexes); negative predictive value 94.2% (91.8% with manual indexes); mean accuracy 92.9% (89.8% with manual indexes).

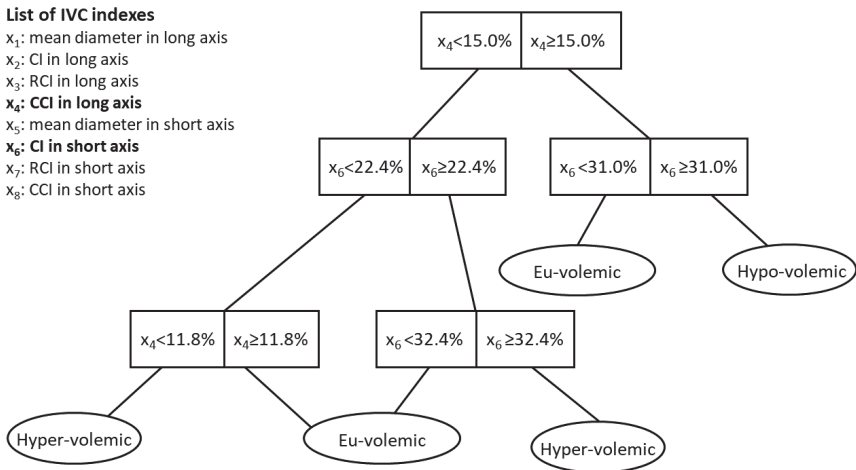


Figure 3. BTM with best performances in fitting our data. The list of tested indexes (all estimated by automated processing) is also provided, with indication (in bold) of those selected by the BTM.

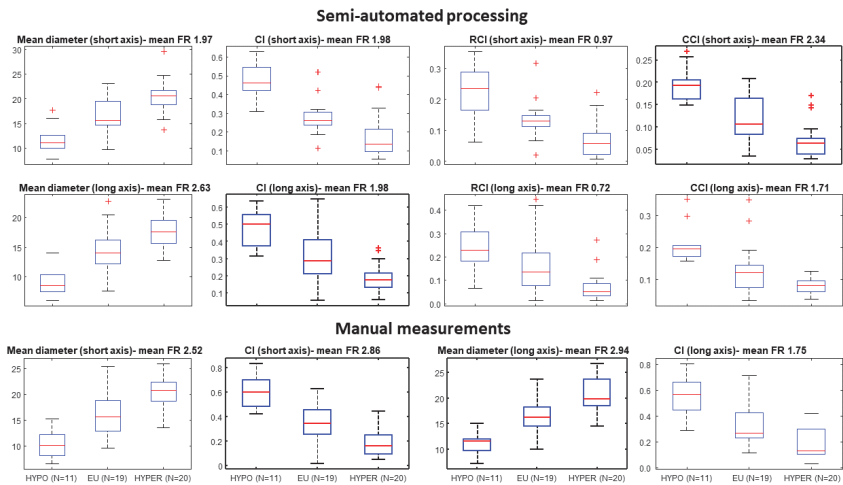


Figure 4. Distribution of the considered IVC indexes from patients with different volemic conditions. The FR (ratio between squared difference of means and sum of variances, computed for all 3 binary comparisons and averaged) is indicated, as an index of linear discrimination. The indexes selected by the best BTMs (those using either semi-automated or manually estimation approach) are emphasized.

Notice that these performances were obtained using the entire dataset to train our model. As some misclassifications were obtained, we deduce that some information is still missing and/or the features extracted by our processing contain some residual noise. To get a more faithful indication of performances, a leave-one-out test was performed (i.e., the best features selected before were kept, but each sample was excluded in turn from the training set and used for testing). The confusion matrix in Table 3 was obtained. Some degradation of the performance can be observed, especially in the discrimination of the control and hyper-volemic groups. The following performance indexes were achieved: mean sensitivity 70.0% (66.0% for the BTM built using the manually estimated indexes and tested by a leave-one-out approach); mean specificity 83.2% (80.4% with manual indexes); positive predictive value 70.0% (65.1% with manual indexes); negative predictive value 82.1% (80.5% with manual indexes); mean accuracy 78.0% (75.3% with manual indexes).

Table 2. Confusion matrix of the best binary tree model classifying the volemic status, shown in Figure 3 (for comparison, the best error-correcting output codes and Naive Bayes classifiers trained on the entire dataset show a predictive value of 78% and 86%, respectively).

Predicted Class	Target Score			Predictive Value
	1: Hypo	2: Eu	3: Hyper	
1	11 (22.0%)	2 (4.0%)	0	84.6%
2	0	15 (30.0%)	1 (2.0%)	93.8%
3	0	2 (4.0%)	19 (38.0%)	90.5%
True rate	100%	78.9%	95.0%	90.0%

Table 3. Confusion matrix obtained by testing the best binary tree model with a leave-one-out approach.

Predicted Class	Target Score			Predictive Value
	1: Hypo	2: Eu	3: Hyper	
1	10 (20.0%)	3 (6.0%)	0	76.9%
2	1 (2.0%)	12 (24.0%)	7 (14.0%)	60.0%
3	0	4 (8.0%)	13 (26.0%)	76.5%
True rate	90.9%	63.2%	65.0%	70.0%

4. Discussion

The accurate assessment of the volume status is of relevance for a high percentage of patients who either access the emergency room or enter the medical wards. The development of new standardized clinical procedures and the support of automatic algorithms can help to correctly plan the treatment and monitor the follow-up.

We have developed two algorithms that help standardizing the assessment of IVC pulsatility. They process B-mode video-clips, allowing to compensate for either longitudinal or transverse respirophasic movements and to delineate the vessel edges in an entire region (either a tract of longitudinal section or a cross-section). As detailed in the Methods section, the IVC indexes extracted are not related to a single diameter along the IVC, but reflect the average size and pulsatility, calculated over the whole portion of considered IVC length (in long axis) or over the entire IVC cross-section (in short axis). Thus, the considered IVC indexes reflect the overall behaviour of the investigated regions (both static and dynamic behaviour, reflected by the size and pulsatility of the IVC, respectively). We have already documented for the long axis scans that this approach is more reliable and repeatable than standard clinical assessment [13,19,25]. Moreover, we have shown that the IVC in a short axis view can pulsate differently along different directions [28], so that an average indication of cross-sectional pulsatility is preferable and less subjective than referring to an arbitrarily chosen diameter.

Here, we have built BTMs using those indexes estimated by our algorithms to assess automatically the volemic conditions of patients. The indexes used by the best BTM reflect IVC pulsatility. Referring to Figure 3, the joint integration of information from CCI from long axis US scans and CI in short axis allows to identify the different conditions, with an accuracy of 78% in a leave-one-out test (larger than what could be achieved with the best classifier using only manual indexes). Notice that CCI is an index that was introduced recently [13,25,37,38] and whose estimation is expected to be stable, as the heartbeats are much less variable than respiratory cycles, mainly affecting the measurements of CI and RCI. Other 4 BTMs achieved the same loss in cross-validation as the best one (which was chosen because it had the smallest dimension). This can be interpreted as a consequence of the redundancy included in the pulsatility indexes, whereby one index may be obtained from a combination of the others. This result may also descend from the small sample size, which does not allow to appreciate fine differences in performance among models with high classification rates. Hence, this should be considered as a pilot study. Augmenting the numerosity of the sample would be important to get a more stable estimation of the classification model.

We have compared the classification performances of the above mentioned fully automated method (based on indexes extracted by processing US B-mode video-clips), with a BTM using indexes measured manually, with M-mode scans along an US ray selected either from a longitudinal or a transverse view of the IVC. It is interesting to notice that the indexes measured manually allowed in general to get a better linear discrimination of the volemic conditions (measured in terms of the average Fisher ratios comparing all pairs of groups). However, the automated processing allowed to extract more indexes describing IVC and the final best classifier showed better performances than that obtained using manual

measurements. In particular, additional information on IVC pulsatility induced by either respiratory cycles or heartbeats was available and CCI (from long axis view) was selected by the best BTM. We deduce that this index includes additional/not redundant information that, together with other characterizations of IVC pulsatility (provided by the CI in short axis, in the best BTM), can be useful to disentangle the complex/nonlinear relation between IVC dynamics and volume status of the patient.

It must be underlined that the present results were obtained from a selected group of patients in which pathologies specifically affecting the respiratory system were excluded. Moreover, we expect that the selection of CCI as optimal feature depends also on the regular heart rhythm shown by the patients included in our dataset; in the case of arrhythmia (typically due to atrial fibrillation, not shown by our data sample), a reliable estimation of this important parameter would be hindered. Thus, the application of our classification approach to different patient populations could result in different selections of parameters and thresholds. Nevertheless, as an effort to overcome the subjectivity of the measurement, our approach (but, probably, not the classification model) remains valid and worth to be investigated and extended to other patients groups.

Another limitation of the method is the need to rely on good quality imaging. Indeed, only 87% and 77% of long and short axis video-clips were properly processed, respectively, so that only 72% of our patients could be included in this study (as the processing of both recordings was required). Improvements could be obtained by adopting higher level US machines or by more effective image processing. We are currently trying to optimize our algorithms in order to process US recordings in real time, providing a feedback to the operator. We expect that this could help in getting successful processing in more US video-clips. Indeed, our present offline approach requires that the operator acquires data blindly, i.e., without knowing if the recorded video-clip will be adequate for processing. Instead, a real time software could guide the acquisition and indicate to the operator if there are problems in processing the data, in which case the operator could work at improving the quality of the imaging. This is exactly what happens in manual measurements: the operator may try different approaches and strategies to improve image quality until he is satisfied with the result and IVC measurement is made possible.

In summary, we have shown the joint application of long and short axis US views of the IVC, to assess the volume status of patients. The US videos have been automatically processed by multi-section and multi-directional algorithms, which track IVC movements and compute its size and pulsatility either over a longitudinal portion of the vessel or a cross-section, respectively. The IVC pulsations have been also split into two contributions, reflecting either the respiratory cycles or the heartbeats. The algorithms have been widely tested on healthy subjects in laboratory conditions in the past [13,19,20,28,29] and in a single clinical study, aimed at estimating right atrial pressure based on the analysis of IVC pulsatility [25,31]. Here, the different indexes were jointly applied in a clinical setting and used to solve the multiclass problem of discriminating patients with different volume status, showing better performance than when using manually measured indexes. Pulsatility indexes estimated from both long and short axis have been included in the best classification model, which supports the concept that they convey complementary information. Even considering the preliminary nature of these results (given the small sample size), the approach appears to be very promising. Extending the dataset and improving the processing algorithms (e.g., allowing real time interaction with the operator) may prospectively lead to obtain efficient systems for diagnostic support and follow-up.

5. Conclusions

The identification of the volume condition is important for the clinical management of many patients in the emergency room or in wards of general medicine and cardiology. We propose an automated approach for the classification of the volemic status, based on the processing of B-mode US video-clips

of the IVC and on the extraction of pulsatility features. The presented results suggest that this approach may be useful to get more reliable clinical indication from the US monitoring of IVC. Investigation over a larger dataset will however be necessary to test the actual effectiveness of the proposed method. Moreover, our results hold true in conditions of normal respiratory function and cardiac rhythm. It is reasonable that our classifier will not apply to patients with more complex cardio-respiratory conditions; however, the same approach could be applied to develop models fitting their conditions.

6. Patents

An instrument implementing the algorithms for IVC delineation used in this paper was patented by Politecnico di Torino and Università di Torino (WO 2018/134726).

Author Contributions: Conceptualization, L.M., S.R., P.P. and M.P.; methodology, L.M.; software, L.M.; validation, L.M.; data preparation, P.P. and M.P.; investigation, L.M. and S.R.; writing—Original draft preparation, L.M.; writing—Review and editing, S.R., M.P., P.P.; visualization, L.M.; supervision, M.P. All authors have read and agreed to the published version of the manuscript.

Funding: This research was carried out as part of the project “Method and apparatus to characterise non-invasively images containing venous blood vessels”, funded through the PoC Instrument initiative, implemented by LINKS, with the support of LIFFT, with funds from Campagna di San Paolo.

Conflicts of Interest: The authors declare no conflict of interest.

Abbreviations

The following abbreviations are used in this manuscript:

BTM	Binary Tree Model
CI	Caval Index
CCI	Cardiac Caval Index
ECOC	Error-Correcting Output Codes
FR	Fisher ratio
IVC	Inferior Vena Cava
RCI	Respiratory Caval Index
SVM	Support Vector Machine
US	Ultrasound

References

1. Alsous, F.; Khamiees, M.; DeGirolamo, A.; Amoateng-Adjepong, Y.; Manthous, C. Negative fluid balance predicts survival in patients with septic shock: A retrospective pilot study. *Chest* **2000**, *117*, 1749–1754. [[CrossRef](#)] [[PubMed](#)]
2. Boyd, J.; Forbes, J.; Nakada, T.; Walley, K.; Russell, J. Fluid resuscitation in septic shock: A positive fluid balance and elevated central venous pressure are associated with increased mortality. *Crit. Care Med.* **2011**, *39*, 259–265. [[CrossRef](#)]
3. Murphy, C.; Schramm, G.; Doherty, J.; Reichley, R.; Gajic, O.; Afessa, B.; Micek, S.; Kollef, M. The importance of fluid management in acute lung injury secondary to septic shock. *Chest* **2009**, *136*, 102–109. [[CrossRef](#)]
4. Dipti, A.; Soucy, Z.; Surana, A.; Chandra, S. Role of inferior vena cava diameter in assessment of volume status: A meta-analysis. *Am. J. Emerg. Med.* **2012**, *30*, 1414–1419. [[CrossRef](#)] [[PubMed](#)]
5. Kelly, N.; Esteve, R.; Papadimos, T.J.; Sharpe, R.P.; Keeney, S.A.; DeQuevedo, R.; Portner, M.; Bahner, D.P.; Stawicki, S.P. Clinician-performed ultrasound in hemodynamic and cardiac assessment: A synopsis of current indications and limitations. *Eur. J. Trauma Emerg. Surg.* **2015**, *41*, 469–480. [[CrossRef](#)] [[PubMed](#)]

6. Yamanoolu, N.G.C.; Yamanoolu, A.; Parlak, Y.; Pynar, P.; Tosun, A.; Erkurun, B.; Aydynok, G.; Torlak, F. The role of inferior vena cava diameter in volume status monitoring; the best sonographic measurement method? *Am. J. Emerg. Med.* **2015**, *33*, 433–438.
7. Ciozda, W.; Kedan, I.; Kehl, D.W.; Zimmer, R.; Khandwalla, R.; Kimchi, A. The efficacy of sonographic measurement of inferior vena cava diameter as an estimate of central venous pressure. *Cardiovasc. Ultrasound* **2016**, *14*, 33. [[CrossRef](#)] [[PubMed](#)]
8. Nagdev, A.; Merchant, R.; Tirado-Gonzalez, A.; Sisson, C.; Murphy, M. Emergency department bedside ultrasonographic measurement of the caval index for noninvasive determination of low central venous pressure. *Ann. Emerg. Med.* **2010**, *55*, 290–295. [[CrossRef](#)]
9. Stawicki, S.P.; Braslow, B.M.; Panebianco, N.L.; Kirkpatrick, J.N.; Gracias, V.H.; Hayden, G.E.; Dean, A.J. Intensivist use of hand-carried ultrasonography to measure IVC collapsibility in estimating intravascular volume status: Correlations with CVP. *J. Am. Coll. Surg.* **2009**, *209*, 55–61. [[CrossRef](#)]
10. Gui, J.; Yang, Z.; Ou, B.; Xu, A.; Yang, F.; Chen, Q.; Jiang, L.; Tang, W. Is the Collapsibility Index of the Inferior Vena Cava an Accurate Predictor for the Early Detection of Intravascular Volume Change? *Shock* **2018**, *49*, 29–32. [[CrossRef](#)]
11. Long, E.; Oakley, E.; Duke, T.; Babl, F.E. Paediatric Research in Emergency Departments International Collaborative (PREDICT). Does Respiratory Variation in Inferior Vena Cava Diameter Predict Fluid Responsiveness: A Systematic Review and Meta-Analysis. *Shock* **2017**, *47*, 550–559. [[CrossRef](#)] [[PubMed](#)]
12. Zhang, Z.; Xu, X.; Ye, S.; Xu, L. Ultrasonographic measurement of the respiratory variation in the inferior vena cava diameter is predictive of fluid responsiveness in critically ill patients: Systematic review and meta-analysis. *Ultrasound Med. Biol.* **2014**, *40*, 845–853. [[CrossRef](#)] [[PubMed](#)]
13. Mesin, L.; Giovinazzo, T.; D'Alessandro, S.; Roatta, S.; Raviolo, A.; Chiacchiarini, F.; Porta, M.; Pasquero, P. Improved repeatability of the estimation of pulsatility of inferior vena cava. *Ultrasound Med. Biol.* **2019**, *45*, 2830–2843. [[CrossRef](#)] [[PubMed](#)]
14. Finnerty, N.M.; Panchal, A.R.; Boulger, C.; Vira, A.; Bischof, J.J.; Amick, C.; Way, D.P.; Bahner, D.P. Inferior Vena Cava Measurement with Ultrasound: What Is the Best View and Best Mode? *West. J. Emerg. Med.* **2017**, *18*, 496–501. [[CrossRef](#)] [[PubMed](#)]
15. Wallace, D.J.; Allison, M.; Stone, M.B. Inferior vena cava percentage collapse during respiration is affected by the sampling location: An ultrasound study in healthy volunteers. *Acad. Emerg. Med.* **2010**, *17*, 96–99. [[CrossRef](#)] [[PubMed](#)]
16. Barbier, C.; Loubieres, Y.; Schmit, C.; Hayon, J.; Ricome, J.L.; Jardin, F.; Vieillard-Baron, A. Respiratory changes in inferior vena cava diameter are helpful in predicting fluid responsiveness in ventilated septic patients. *Intensive Care Med.* **2004**, *30*, 1740–1746. [[CrossRef](#)]
17. Blehar, D.J.; Dickman, E.; Gaspari, R. Identification of congestive heart failure via respiratory variation of inferior vena cava diameter. *Am. J. Emerg. Med.* **2009**, *27*, 71–75. [[CrossRef](#)]
18. Blehar, D.; Resop, D.; Chin, B.; Dayno, M.; Gaspari, R. Inferior vena cava displacement during respirophasic ultrasound imaging. *Crit. Ultrasound J.* **2012**, *4*, 1–5. [[CrossRef](#)]
19. Mesin, L.; Pasquero, P.; Albani, S.; Porta, M.; Roatta, S. Semi-automated tracking and continuous monitoring of inferior vena cava diameter in simulated and experimental ultrasound imaging. *Ultrasound Med. Biol.* **2015**, *41*, 845–857. [[CrossRef](#)]
20. Mesin, L.; Pasquero, P.; Roatta, S. Tracking and Monitoring Pulsatility of a Portion of Inferior Vena Cava from Ultrasound Imaging in Long Axis. *Ultrasound Med. Biol.* **2019**, *45*, 1338–1343. [[CrossRef](#)]
21. Bouzat, P.; Walther, G.; Rupp, T.; Levy, P. Inferior Vena Cava Diameter May Be Misleading in Detecting Central Venous Pressure Elevation Induced by Acute Pulmonary Hypertension. *Am. J. Respir. Crit. Care Med.* **2014**, *190*, 233–235. [[CrossRef](#)] [[PubMed](#)]
22. Inocencio, M.; Childs, J.; Chilstrom, M.L.; Berona, K. Ultrasound Findings in Tension Pneumothorax: A Case Report. *J. Emerg. Med.* **2017**, *52*, e217–e220. [[CrossRef](#)] [[PubMed](#)]
23. Hjemdahl-Monsen, C.E.; Daniels, J.; Kaufman, D.; Stern, E.H.; Teichholdt, L.E.; Meltzer, R.S. Spontaneous contrast in the Inferior vena cava in a patient with constrictive Pericarditis. *J. Am. Coll. Cardiol.* **1984**, *4*, 165–167. [[CrossRef](#)]

24. Pellicori, P.; Carubelli, V.; Zhang, J.; Castiello, T.; Sherwi, N.; Clark, A.L.; Cleland, J.G.F. IVC diameter in patients with Chronic Heart Failure: Relationships and prognostic significance. *J. Am. Coll. Cardiol. Cardiovasc. Imaging* **2013**, *6*, 16–28. [\[CrossRef\]](#) [\[PubMed\]](#)
25. Mesin, L.; Albani, S.; Sinagra, G. Non-invasive Estimation of Right Atrial Pressure using the Pulsatility of Inferior Vena Cava. *Ultrasound Med. Biol.* **2019**, *45*, 1331–1337. [\[CrossRef\]](#)
26. Lichtenstein, D. *Inferior Vena Cava. General Ultrasound in the Critically Ill*; Springer: Berlin, Germany, 2005; Volume 23, p. 82.
27. Huguet, R.; Fard, D.; d’Humieres, T.; Brault-Meslin, O.; Faivre, L.; Nahory, L.; Dubois-Randé, J.; Ternacle, J.; Oliver, L.; Lim, P. Three-dimensional inferior vena cava for assessing central venous pressure in patients with cardiogenic shock. *J. Am. Soc. Echocardiogr.* **2018**, *31*, 1034–1043. [\[CrossRef\]](#)
28. Mesin, L.; Pasquero, P.; Roatta, S. Multi-directional assessment of Respiratory and Cardiac Pulsatility of the Inferior Vena Cava from Ultrasound Imaging in Short Axis. *Ultrasound Med. Biol.* **2020**, in press. [\[CrossRef\]](#)
29. Folino, A.; Benzo, M.; Pasquero, P.; Laguzzi, A.; Mesin, L.; Messere, A.; Porta, M.; Roatta, S. Vena Cava Responsiveness to Controlled Isovolumetric Respiratory Efforts. *J. Ultrasound Med.* **2017**, *36*, 10, 2113–2123. [\[CrossRef\]](#)
30. Magnino, C.; Omedé, P.; Avenatti, E.; Presutti, D.; Iannaccone, A.; Chiarlo, M.; Moretti, C.; Gaita, F.; Veglio, F.; Milan, A. RIGHT1 Investigators. Inaccuracy of right atrial pressure estimates through inferior vena cava indices. *Am. J. Cardiol.* **2017**, *120*, 1667–1673. [\[CrossRef\]](#)
31. Albani, S.; Pinamonti, B.; Giovinazzo, T.; de Scordilli, M.; Fabris, E.; Stolfo, D.; Perkan, A.; Gregorio, C.; Barbati, G.; Geri, P.; et al. Accuracy of right atrial pressure estimation using a multi-parameter approach derived from inferior vena cava semi-automated edge-tracking echocardiography: A pilot study in patients with cardiovascular disorders. *Int. J. Cardiovasc. Imaging* **2020**, *36*, 1213–1225. [\[CrossRef\]](#)
32. Bevilacqua, V.; Dimauro, G.; Marino, F.; Brunetti, A.; Cassano, F.; Maio, A.; Nasca, E.; Trotta, G.F.; Girardi, F.; Ostuni, A.; et al. A novel approach to evaluate blood parameters using computer vision techniques. In Proceedings of the IEEE International Symposium on Medical Measurements and Applications (MeMeA), Benevento, Italy, 15–18 May 2016; pp. 1–6.
33. Khurram, I.Q.; Lam, H.K.; Bo, X.; Gaoxiang, O.; Xunhe, Y. Classification of epilepsy using computational intelligence techniques. *CAAI Trans. Intell. Technol.* **2016**, *1*, 2, 137–149.
34. Furnkranz, J. Round Robin Classification. *J. Mach. Learn. Res.* **2002**, *2*, 721–747.
35. Trevor, H.; Tibshirani, R.; Friedman, J. *The Elements of Statistical Learning*; Springer Series in Statistics; Springer: New York, NY, USA, 2008.
36. Varma, S.; Simon, R. Bias in error estimation when using cross-validation for model selection. *BMC Bioinform.* **2006**, *7*, 91.
37. Nakamura, K.; Tomida, M.; Ando, T.; Sen, K.; Inokuchi, R.; Kobayashi, E.; Nakajima, S.; Sakuma, I.; Yahagi, N. Cardiac variation of inferior vena cava: New concept in the evaluation of intravascular blood volume. *J. Med. Ultrasound* **2013**, *40*, 205–209. [\[CrossRef\]](#) [\[PubMed\]](#)
38. Sonoo, T.; Nakamura, K.; Ando, T.; Sen, K.; Maeda, A.; Kobayashi, E.; Sakuma, I.; Doi, K.; Nakajima, S.; Yahagi, N. Prospective analysis of cardiac collapsibility of inferior vena cava using ultrasonography. *J. Crit. Care* **2015**, *30*, 945–948. [\[CrossRef\]](#) [\[PubMed\]](#)



MDPI
St. Alban-Anlage 66
4052 Basel
Switzerland
Tel. +41 61 683 77 34
Fax +41 61 302 89 18
www.mdpi.com

Electronics Editorial Office
E-mail: electronics@mdpi.com
www.mdpi.com/journal/electronics



MDPI
St. Alban-Anlage 66
4052 Basel
Switzerland

Tel: +41 61 683 77 34
Fax: +41 61 302 89 18

www.mdpi.com



ISBN 978-3-0365-0347-9